Non-invasive measurement of intra-tumoral fluid dynamics with localized convolutional function regression

Authors: Ryan T. Woodall*[1], Cora C. Esparza[2], Margarita Gutova[3], Maosen Wang[2], Jessica Cunningham-Reynolds[2], Alexander Brummer[4], Caleb Stine[2], Christine C. Brown[5,6], Jennifer M. Munson*[2], Russell C. Rockne*[1]

Affiliations:

[1]Division of Mathematical Oncology and Computational Systems Biology, Department of Computational and Quantitative Medicine, Beckman Research Institute, City of Hope National Medical Center; 1500 E Duarte Rd, Duarte, CA 91010, USA.

[2]Fralin Biomedical Research Institute, Virginia Technical Institute at Virginia Tech Carilion, Virginia Tech, 4 Riverside Circle, Roanoke, VA 24016, USA

[3]Department of Stem Cell Biology and Regenerative Medicine Beckman Research Institute, City of Hope National Medical Center; 1500 E Duarte Rd, Duarte, CA 91010, USA.

[4]Department of Physics and Astronomy, College of Charleston; 66 George Street, Charleston, SC 29424, USA

[5]Hematology & Hematopoietic Cell Transplantation, Beckman Research Institute, City of Hope National Medical Center; 1500 E Duarte Rd, Duarte, CA 91010, USA.

[6]Department of Immuno-Oncology, Beckman Research Institute, City of Hope National Medical Center; 1500 E Duarte Rd, Duarte, CA 91010, USA.

Corresponding authors*: Ryan T. Woodall, Jennifer M. Munson, Russell C. Rockne

Email: rwoodall@coh.org, munsonj@vt.edu, rrockne@coh.org

Abstract: Dynamic contrast-enhanced magnetic resonance imaging (DCE-MRI) is a routine method to non-invasively quantify perfusion dynamics in tissues. The standard practice for analyzing DCE-MRI data is to fit an ordinary differential equation to each voxel. Recent advances in data science provide an opportunity to move beyond existing methods to obtain more accurate measurements of fluid properties. Here we present localized convolutional function regression, simultaneously measuring interstitial fluid velocity, diffusion, and perfusion in 3D. We validate the method computationally and experimentally, demonstrating accurate measurement of fluid dynamics in situ and in vivo. Applying the method to human MRIs, we observe tissue-specific differences in fluid dynamics, with an increased fluid velocity in breast cancer as compared to brain cancer.

One-Sentence Summary: A physics-informed computational method enables accurate and efficient measurement of fluid dynamics in individual patient tumors and demonstrates differences between tissues.

Main Text:

Interstitial fluid transport is intrinsically linked to the movement of drugs, nutrients, and cells in tissues and is especially important for understanding cancer physiology. Cancers in any tissue develop aberrant transport that can affect the movement of drugs into and through tumors. Interstitial fluid flow, in particular, has been identified as a driving force in tumor cell invasion into surrounding healthy tissue (*1–4*). Interstitial flow can also change the surrounding microenvironment, activating fibroblasts (*5*, *6*), directing immune cell behavior (*7*, *8*), and inducing angiogenesis (*9*, *10*). Better measurement and mapping of interstitial flows and interstitial transport may offer insight into disease progression and therapeutic application strategies (*11*, *12*), though measuring the interstitial fluid flow field non-invasively has remained a challenge, particularly in situ and in 3D.

Contrast-enhanced magnetic resonance imaging (MRI) has provided clinical benefit for cancer treatment for many decades (*13*). Due to the enhanced permeability and retention effect in tumors and the breakdown of the blood-brain-barrier, MR contrast agent preferentially leaks from tumor-associated vasculature, enabling identification of brain tumors and the quantification of blood dynamics within tumors. Because of this, MRI has become a staple of diagnosing, planning, and providing prognosis in several cancer settings (*14–16*).

In 1999, Tofts et. al released their work on compartmental models of dynamic MRI, shifting the paradigm from static pre- and post-contrast MRI, to dynamic contrast-enhanced (DCE-MRI) (*17*). For physical interpretation of contrast enhancement data, researchers have taken to processing the data on an individual voxel basis. While there are a wide variety of ordinary differential equation (ODE) models, each with their own strengths and limitations, ODE-based approaches largely fail to incorporate the rich spatial data provided by the modality (*18*). Few methods exist for quantifying the spatially varying effective diffusion coefficient of contrast agent in DCE-MRI (*19*, *20*), and even fewer attempt to quantify and investigate interstitial fluid flow (i.e. advection) within the tumor (*21–23*). While there exist MR sequences which attempt to measure interstitial fluid velocity (*24*, *25*), they largely remain research tools.

As the spatial and temporal resolution of DCE-MRI has increased and acquisition protocols become more standardized, the field of data science has matured significantly (*26*, *27*). One important advancement in the field, published by Brunton and Kutz (2017), is their method for sparse identification of nonlinear dynamics (SINDy), which allows for the discovery of equations governing time-series data through the concept of function-space regression (*28*). While extremely effective at analyzing smooth and densely-sampled data, this method would require modification to be applied successfully to DCE-MRI data, where the temporally and spatially resolved data is often noisy (*29*). Weak SINDy is a method proposed by Messenger and Bortz, which leverages the weak form of governing equations to provide an efficient and accurate method for simultaneous model discovery and parameter estimation from noisy data (*30*). Weak derivatives are the backbone of modern computational fluid dynamics, transforming ordinary or partial differential equations into linear matrix equations, where solutions are constructed from localized basis functions (*31*). Instead of taking a finite-difference approximation of the derivative, Messenger and Bortz suggest raw data be integrated with derivatives of a known basis function, selected by the user to be optimal for the problem at hand. Basis functions are selected such that they possess analytical expressions for derivatives, and can be constructed from polynomials (*30*). This method bypasses the use of discrete approximations of derivatives on noisy or sparse data, which are used by SINDy (*28*), or iterative gradient descent methods used in modern DCE-MRI model inversion which require estimating derivatives of the objective function with respect to the data (*21–23*).

Here we tailor weak SINDy for partial differential equations (PDEs) to DCE-MRI, performing localized convolutional function regression (LCFR) to recover spatially localized fluid transport parameters (Fig. 1, A). Briefly, it is assumed that the dynamics of contrast agent transport are governed by an advection-diffusion-reaction PDE, with vascular input forcing function (VIF), and an unmixed enhancing plasma-compartment (v_p), consistent with extended Tofts-Kety intra-voxel transport (K^{trans}, K^{ep}), advective ($\vec{u}$) and diffusive (D) inter-voxel transport:

(1)

$$\partial_t c = \nabla \cdot (D\nabla c) - \nabla \cdot (\vec{u} \cdot c) + K^{trans} VIF - K^{ep} c + v_p \partial_t VIF$$

We then project the concentration of contrast agent, $c(\boldsymbol{X}, t)$, onto smooth, 4D polynomial basis functions $\Psi(\boldsymbol{X}, t)$, to perform a spatially localized model regression of the form:

(2)

$$\tilde{c}_t = \Theta\big(c(\boldsymbol{X}, t), VIF(X, t)\big)\, \Xi$$

where ~ indicates convolution of the data onto basis functions or their derivatives, denoted as $\tilde{f} = \langle f(\boldsymbol{X}, t), \Psi(\boldsymbol{X}, t)\rangle$ and $\tilde{f}_q = -\langle f(\boldsymbol{X}, t), \partial_q \Psi(\boldsymbol{X}, t)\rangle$, respectively (Supplemental Equation 21-22). The model regression problem is then formulated on a (x, y, z) 3x3x3 window where a weak derivative of the data is performed via the basis functions. The matrix $\Theta\big(c(\boldsymbol{X}, t), VIF(\boldsymbol{X}, t)\big)$ is populated with polynomial projections of the data and corresponding weak derivatives, $\Theta = [\tilde{c}_{xx}, \tilde{c}_{yy}, \tilde{c}_{zz}, \tilde{c}_x, \tilde{c}_y, \tilde{c}_z, \tilde{c}, \widetilde{VIF}, \widetilde{VIF}_t]$. The model regression problem is then solved locally in space, for all time, to recover the vector Ξ, which consists of coefficients of the governing equation (1) as, $\Xi = \left[\xi_{D,x}, \xi_{D,y}, \xi_{D,z}, \xi_{u,x}, \xi_{u,y}, \xi_{u,z}, \xi_{ep}, \xi_{trans}, \xi_{VIF}\right]^T$. A mapping between the coefficients and the terms of the full expansion of equation (1) can be found in the Supplement (S14, S15).

We validate the method in silico, and experimentally in a hydrogel model. Further, we demonstrate our method in vivo with a mouse xenograft model and demonstrate the clinical potential by examining fluid dynamics in human glioblastoma brain tumors and breast cancer data sets (*32*, *33*).

Results

LCFR accurately estimates transport parameters from in silico phantoms

We first demonstrate the ability of our methodology to recover local PDE coefficients in silico from forward model simulations. An advection-diffusion model is used to generate two flow patterns (Supplemental Table 1). The first model is a radially diverging flow field (Fig. 1, B), and the second model is a Poiseuille shear flow (Fig. 1, C). In both cases, LCFR accurately recovers the direction and magnitude of the flow field after addition of 0.1% noise (% maximum signal), with root mean squared error (RMSE) for divergent flow RMSE = 1.02E-1 mm/s, and RMSE = 4.63E-1 mm/s for Poiseuille flow. Edge effects due to the Gibbs phenomenon resulting from the Fourier transform to compute the convolution with the basis functions are removed from the visualization and analysis.

To test the ability of the method to identify the transport rate constant K^{trans} and vascular volume fraction v_p, we simulate the extended Tofts-Kety dynamics with spatially varying perfusion and 0.1% noise, K^{trans}, and constant vascular volume fraction, v_p = 5.00E-2. In this scenario, K^{trans} is accurately estimated by the coefficient ξ_{trans} (RMSE = 1.54E-1 1/s), while the measurement of the plasma volume fraction v_p (RMSE = 3.89E-1) is observed to be influenced by the transport rate K^{trans} (**Table S1, Figure S3**).

LCFR accurately measures the mean contrast velocity in porous hydrogel

We next validate the methodology in vitro, by administering a bolus of contrast agent on top of porous hydrogel with a pressure head forcing the contrast agent through the gel (Fig. 2, A). DCE-MRI is acquired at 30 second time intervals, signal intensity is converted to contrast agent concentration using T1-mapping, and LCFR is applied to the resulting concentration field. We manually estimate the velocity of the contrast agent front ($|\vec{u}|$ =1.14E-3 mm/s) (Fig 2. B) and compare it to the LCFR-estimated 3D velocity $|\overrightarrow{\xi_u}|$ within the hydrogel ($|\overrightarrow{\xi_u}|$ =1.32E-3 ± 8.20E-4 mm/s) (Fig 2, B-E). The mean measured diffusivity within the gel $\xi_{\bar{D}}$ was measured to be $\xi_{\bar{D}}$ =1.48E-4 ± 7.35E-6 mm^2/s (N = 3). This analysis was performed on multiple replicates, and the mean error associated with the method was 15.2% ± 1.08% (N = 3) (Fig 2. E).

LCFR-measured perfusion predicts Evans Blue leakage into tumors in vivo

We subsequently validated the method in vivo. Six mice (N = 6) implanted with GFP-GL261 cells to the brain underwent DCE-MRI with isotropic spatial resolution of 0.2 mm, at 7 and 14 days post-implantation. The measured velocity $|\overrightarrow{\xi_u}|$ remained constant from $|\overrightarrow{\xi_u}|$ =1.35E-3 ± 7.04E-4 mm/s on day 7, to $|\overrightarrow{\xi_u}|$ =1.63E-3 ± 4.04E-4 mm/s on day 14 (P = 0.218, N = 6, two-tailed Wilcoxon test) (Fig 2, H). The fluid rate transfer constant, ξ_{trans}, increased from 2.70E-2 ± 8.65E-3 1/s on day 7, to 5.08E-2 ± 1.84E-2 1/s on day 14 (P = 0.063, N = 6, two-tailed Wilcoxon test) (Fig 3, I). After imaging on day 14, the mice were injected with Evans Blue to quantify perfusion, and brains were harvested and stained for visual comparison to LCFR outputs (Fig. 3, A through D). The mean Evans Blue coverage within the tumor was observed to be positively correlated with the mean tumor perfusion rate constant, ξ_{trans}, across all mice (r = 0.507, P = 0.038, N = 17, two-tailed Pearson correlation) (Fig. 3, H). The resulting 3D interstitial velocity field, $\overrightarrow{\xi_u}$, is displayed over the native post-contrast T1 weighted volume, highlighting that LCFR is readily applied on 4D data (Fig 3, G).

LCFR-measured interstitial fluid velocity varies between breast and brain cancer

To investigate the differences in interstitial fluid flow between cancer in different tissues, we applied LCFR to clinical DCE-MRI in a cohort of glioblastoma patients, and a cohort of breast cancer patients. In the glioblastoma cohort, 20 patients with recurrent disease who underwent DCE-MRI imaging between January 2020, and July 2022 were selected from the radiology records at City of Hope National Medical Center. The glioblastoma patients underwent DCI-MRI from on average = 32.3 days after resection and prior to receiving additional therapy The breast cancer cohort consisted of 13 treatment-naïve patients from the Quantitative Imaging Network BREAST-02 study (*33*). In these cohorts, we measured the flow velocity, $|\overrightarrow{\xi_u}|$, in breast tumors (1.03E-1 ± 3.10E-2 mm/s) to be significantly faster than that in brain tumors (6.81E-2 ± 1.99E-2 mm/s) (P < 0.001, N_{brain} = 20, N_{breast} = 13, two-tailed Mann Whitney test).

Discussion

Here we present a novel methodology for analyzing DCE-MRI data, which allows for accurate, non-invasive measurement of fluid dynamics in living tissues. The methodology leverages the rich spatial and temporal data provided by DCE-MRI to enhance our understanding of tissue fluid dynamics. We have validated our approach using synthetic and experimental data and demonstrate its application to human MRI data routinely collected in the clinic.

Our in silico validation demonstrates the ability of our method to accurately capture both the direction and magnitude of different fluid velocity fields (Fig 1, B and C). Sharp changes in the field are smoothed out by the basis functions, though the resulting fields are consistent with the true velocity fields. We also demonstrate measurement of Tofts-Kety-like dynamics (Fig S3), wherin ξ_{trans} accurately estimates K^{trans}.

When used on DCE-MRI data, LCFR can accurately measure the mean 3D flow velocity of contrast agent forced through a hydrogel in a trans-well, comparing the apparent velocity of the contrast agent front to that measured by the parameter $|\overrightarrow{\xi_u}|$, resulting in an average error of 15.2% ± 1.08% (N = 3). Further, the mean diffusivity in the gel, $\xi_{\overline{D}}$, is consistent with diffusivity measurements reported in vivo and in hydrogel (*34*, *35*). Given the accuracy of the advection and diffusion coefficients in simulation and in hydrogel, we have confidence the differences in fluid velocity $|\overrightarrow{\xi_u}|$ measured in brain and breast tissues is reliably measured and reflects differences in the underlying biology and tissue structure, which may be explained by the differences in tissue density and perfusion in each of these organs.

Recent studies have used phase-contrast imaging to directly measure fluid velocity within tumors (*24*, *25*). Zhao et. al measured the mean tumor fluid velocity magnitude in mice as 1.13E-1 ± 24E-4 mm/s, and Walker-Samuel et al. reported 1.10E-1 ± 5.5E-4 mm/s. In our studies, the mean estimated velocity magnitude in mice was 1.35E-3 ± 7.04E-4. In both Zhao et. al and Walker-Samuel et. al, this measurement is described as higher than previous literature values, attributing this difference to contribution from vascular flow, which could not be disambiguated from tissue interstitial fluid flow (*24*, *25*). In the present study, the bolus arrival time is corrected for in each voxel, thus minimizing the contribution of vascular velocity in the total velocity field. Further, the studies cited by Zhao et al. and Walker-Samuel et. al employ IFF estimation methods which are not consistent with the experimental assumptions present for sub-minute time-resolution, such as assuming that the pressure in the tumor is spatially uniform (*36*), or measuring the radius of enhancement at a long time-scale (60 min.) (*37*). Additionally, we demonstrate (Supplemental Equation 14) that the spatial gradient of diffusion is structurally unidentifiable from true advective transport and may thus artificially increase the apparent velocities observed in this study, and others directly measuring advective transport. These confounding factors may contribute to higher apparent velocities measured by methods which utilize higher temporal resolution data, or do not account for diffusive and advective transport separately.

Our methodology comes with significant advantages over traditional model inversion methods used to parameterize DCE-MRI data, foremost that it is readily applied in native 4D, instead on individual z-slices, allowing for simultaneous estimation of both inter- and intra-voxel fluid transport parameters,. Further, LCFR is robust to noise due to the use of smooth polynomial basis functions. Our method is highly efficient, utilizing the fast Fourier Transform for convolution with basis functions, and linear regression for the recovery of local PDE coefficients. Finally, our method allows for a direct calculation of parameters of a PDE from the original data, without the need for iterative forward-PDE solutions required for PDE inverse problems (*38*, *39*). While these

advantages are useful for this type of data, they do come with trade-offs which limit the performance of the method.

Our method utilizes a pre-defined library of functions to characterize the dynamics (Θ), instead of an extensive library of hypothetical functions and polynomial combinations of partial derivatives. This is largely because neither the higher-order and spatial cross-derivatives, nor products of these terms would not be readily interpretable with respect to the physics at hand, and storage of each of these 4D arrays may be memory-expensive. Additionally, we utilize L2 regression for simplicity and efficiency, as opposed to sparse objective functions such as LASSO or SR3, which are typically utilized in model discovery frameworks (*30*, *40*). For this reason, we refer to our method as function regression, instead of model discovery. Some of the PDE parameters are unidentifiable given the structure of the underlying PDE and characteristics of the vascular input function. Further, due to the nature of any overdetermined regression problem, the models recovered may not be unique. This is especially the case for model discovery methods which utilize L1 or SR3, as the discovered model strongly depends on the sparsity parameters used to enforce parsimony. While the present methods may not yield unique results for each individual spatial window, these results consistently indicate the presence of directed transport within tumors and allow for the accurate measurement of transport parameters in vitro and within living tissue.

Conclusion

In this work, we present a model-regression framework tailored specifically to the unique needs of DCE-MRI, utilizing advances made in the model discovery field to adapt to noisy data. This methodology is experimentally validated on simulated data, and experimentally on a porous hydrogel. In an in vivo mouse study, we capture changes in tumor perfusion and interstitial flow over time and find that perfusion estimated by this non-invasive method are consistent with measures of perfusion and vascular density measured from tissue histology. Finally, we measure fluid velocity magnitude in brain and breast cancers and find the velocity to be greater in breast than brain, suggesting differences in underlying biology and demonstrating the application of this novel methodology to routinely collected clinical imaging.

Acknowledgments: The authors would like to thank the clinicians and researchers who contributed to the creation of the Quantitative Imaging Network Breast-02 and Prostate datasets, and the City of Hope neuro-oncology program. We especially thank all the patients who voluntarily participated in the QIN studies, and their families, for their exemplary strength and generosity. We could not have performed this research without you.

Funding Research reported in this publication was supported by the National Institutes of Health under award numbers P30CA033572, R01NS115971 (R.C.R., C.E.B., J.M.) R01CA254271 (C.E.B.) and the California Institute for Regenerative Medicine under award CLIN2-10248 (C.E.B.). The content is solely the responsibility of the authors and does not necessarily represent the official views of the National Institutes of Health or the California Institute of Regenerative Medicine.

IRB Statement The study of publicly available data and retrospective analysis of City of Hope patient data was approved with a waiver of consent by the local Institutional Review Board Protocol 15286.

Author contributions:

Conceptualization: RTW, JRC, JMM, RCR

Methodology: RTW, MW, JCR, RCR, JMM, ABB

Investigation: RTW, CCE, MW

Visualization: RTW, CCE, JRC, JMM, RCR

Funding acquisition: RCR, CCB, JMM

Project administration: RCR, JMM, CCB

Supervision: RCR, JMM, RTW, CCB

Writing – original draft: RTW

Writing – review & editing: RTW, CCE, JCR, MW, MG, CCB, ABB, CS, JMM, RCR

Competing interests: The methodologies described herein are disclosed and claimed in a pending patent application co-owned by City of Hope and Virginia Polytechnic Institute and State University listing RTW, JRC, RCR, and JMM as co-inventors. RTW, JRC, CS, RCR, and JMM own stake in Cairina Inc.

Data and materials availability: The raw data for analysis, forward models for in silico validation, and raw-output of the LCFR-processed data shown in this work are provided for review. All data and code will be made readily available to readers upon request to the corresponding authors.

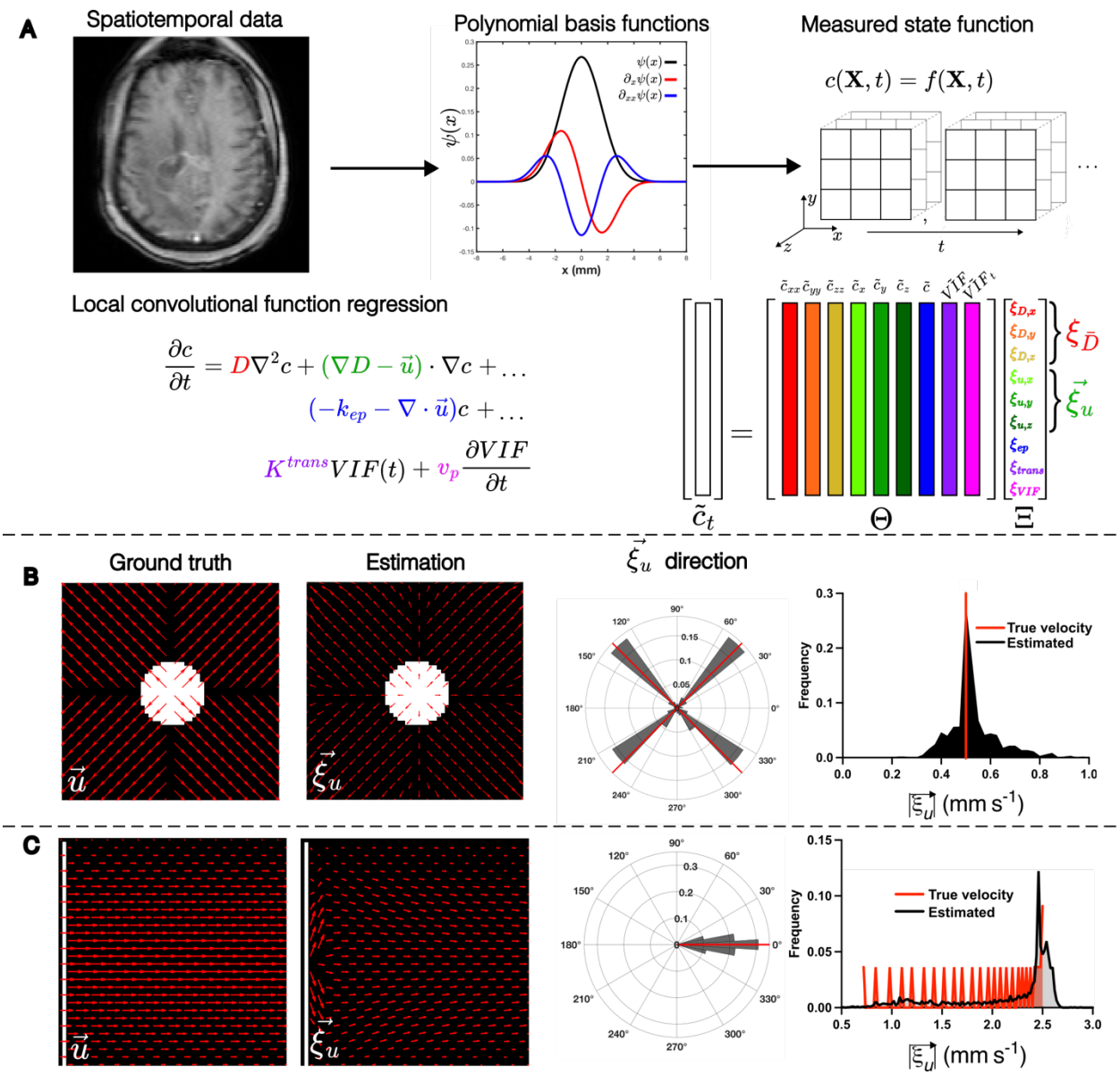

Figure 1: LCFR Methodology and validation with in silico phantoms. (A) Methodology of Localized Convolutional Function Regression (LCFR), wherein spatiotemporal contrast agent concentration data is convolved with a smooth basis-function and its derivatives, divided into 3x3x3 windows. The coefficients of the factored transport PDE are then solved for using linear regression. (B) Validation of LCFR coefficient $\vec{\xi}_u$ on a divergent flow field (initial condition, white) with spatially invariant diffusion, and the true direction and magnitude of velocity denoted in red bars. (C) Validation of CLFR on a Poiseuille shear flow field with spatially invariant diffusion (initial condition, white), and the true direction and magnitude of velocity denoted in red bars.

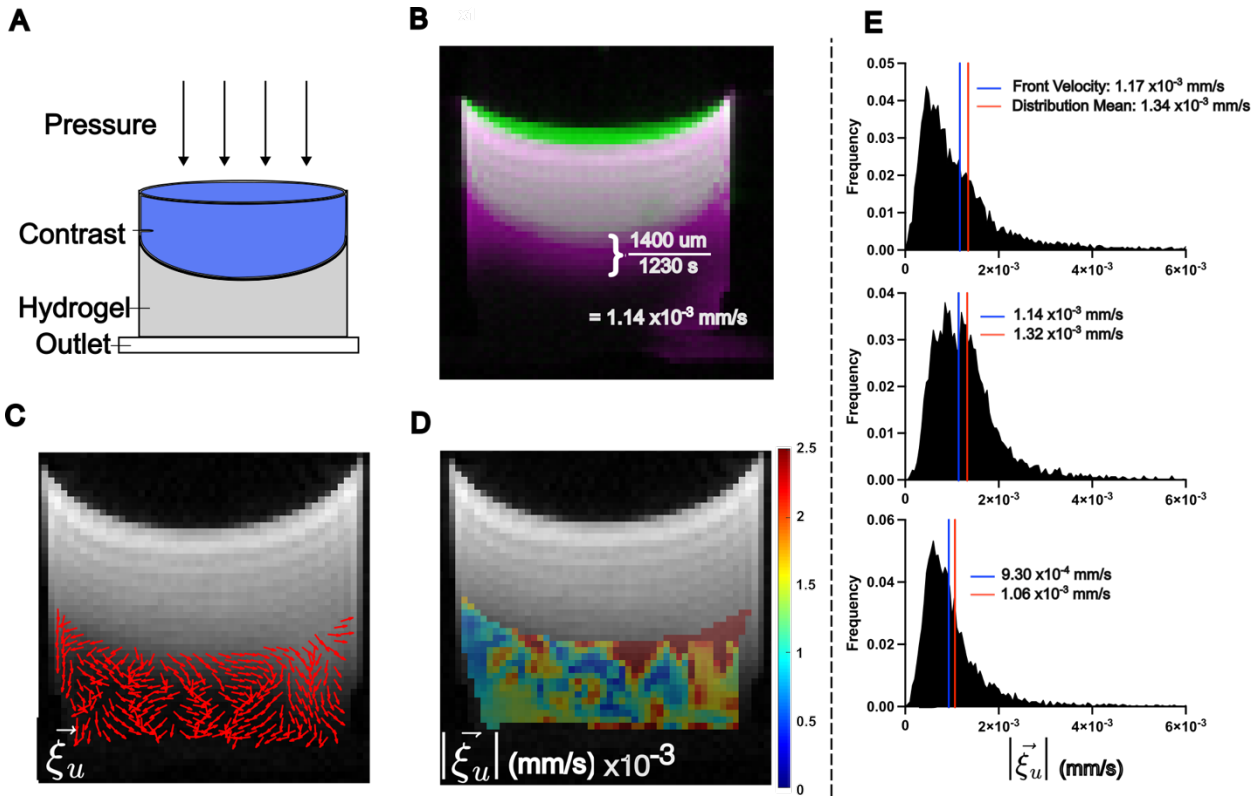

Figure 2: LCFR predicts interstitial fluid velocity in hydrogel phantoms. (A) Experimental setup, wherein a bolus of contrast agent is administered onto of a porous hydrogel and drains through due to a hydraulic pressure head. (B) Method of estimating the mean flow velocity of the contrast agent front, using the difference between the initial contrast location (green), and final contrast location (pink), resulting in an estimated contrast agent velocity of 1.14E-3 mm/s. (C) The estimated in-plane interstitial flow velocity direction overlaid on the final T1-weighted image. (D) The local 3D magnitude of interstitial flow velocity within the hydrogel. (E) Histograms of three replicate trials, comparing the 3D magnitude of flow velocity within the hydrogel, with blue line indicating the estimated contrast front velocity, and red line indicating the mean velocity of the distribution as measured by LCFR.

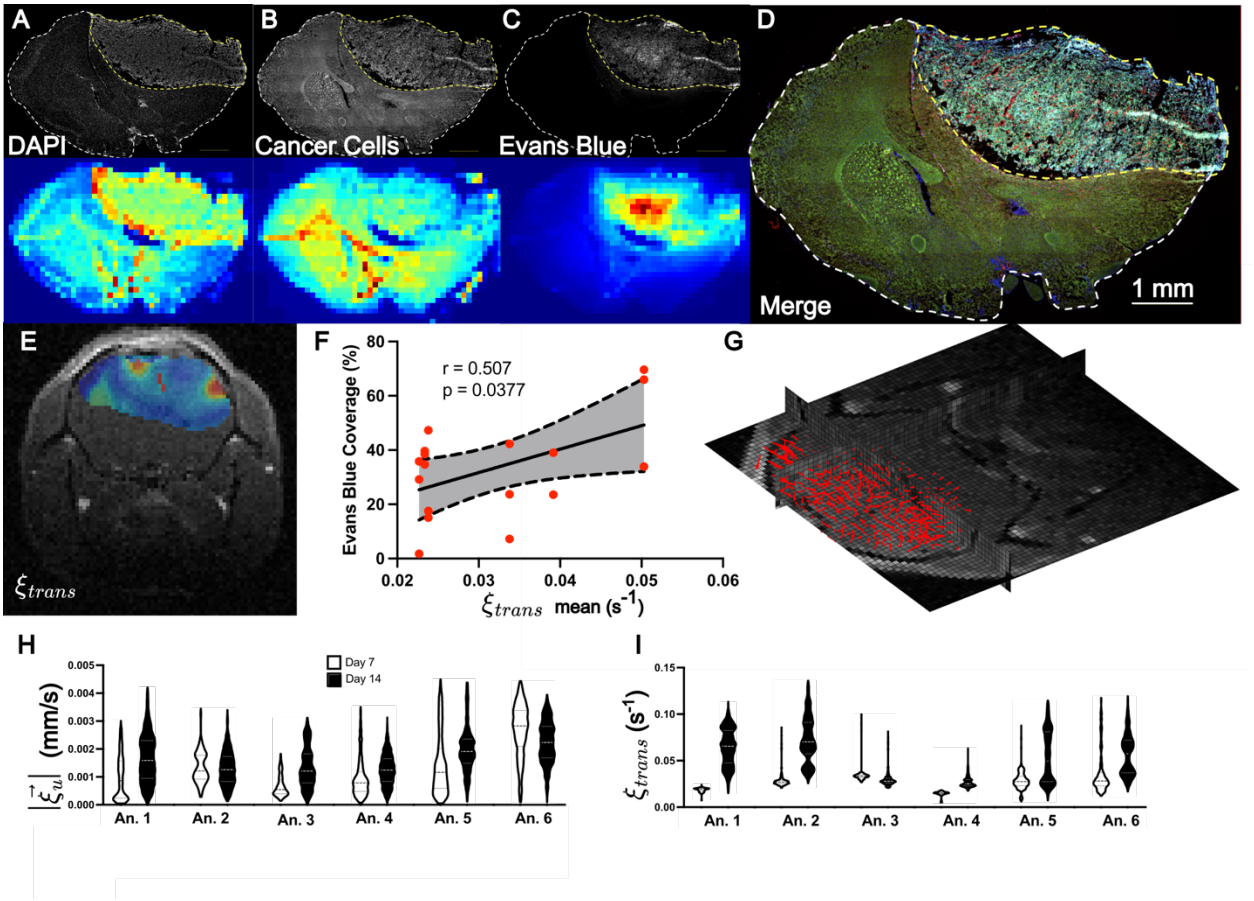

Figure 3: LCFR-measured perfusion is correlated to Evans Blue coverage in vivo. (A through D) Representative coronal IHC stains through the central tumor slice (top row), and MR resolution-matching intensity projection (bottom row), consisting of DAPI (A), GFP-expressing GL261 cells (B), Evans Blue (C). (D) Merge of all IHC demonstrating tumor heterogeneity. (E) Estimated perfusion field, ξ_{trans}, overlaid on post-contrast T1-weighted image. (F) Scatter plot depicting the correlation and 95% confidence interval of linear regression between mean tumor perfusion as measured by DCE-MRI (ξ_{trans}, x-axis), and Evans Blue Coverage (mean tumor stain intensity, y-axis), for n = 17 histology slices. (G) 3D velocity vector field of estimated interstitial velocity $\vec{\xi_u}$, overlaid on the 3D T1 post-contrast volume. (H and I) Violin plots depicting the estimated velocity magnitude (H) and perfusion (I) for 6 animals imaged 7 and 14 days after tumor implantation.

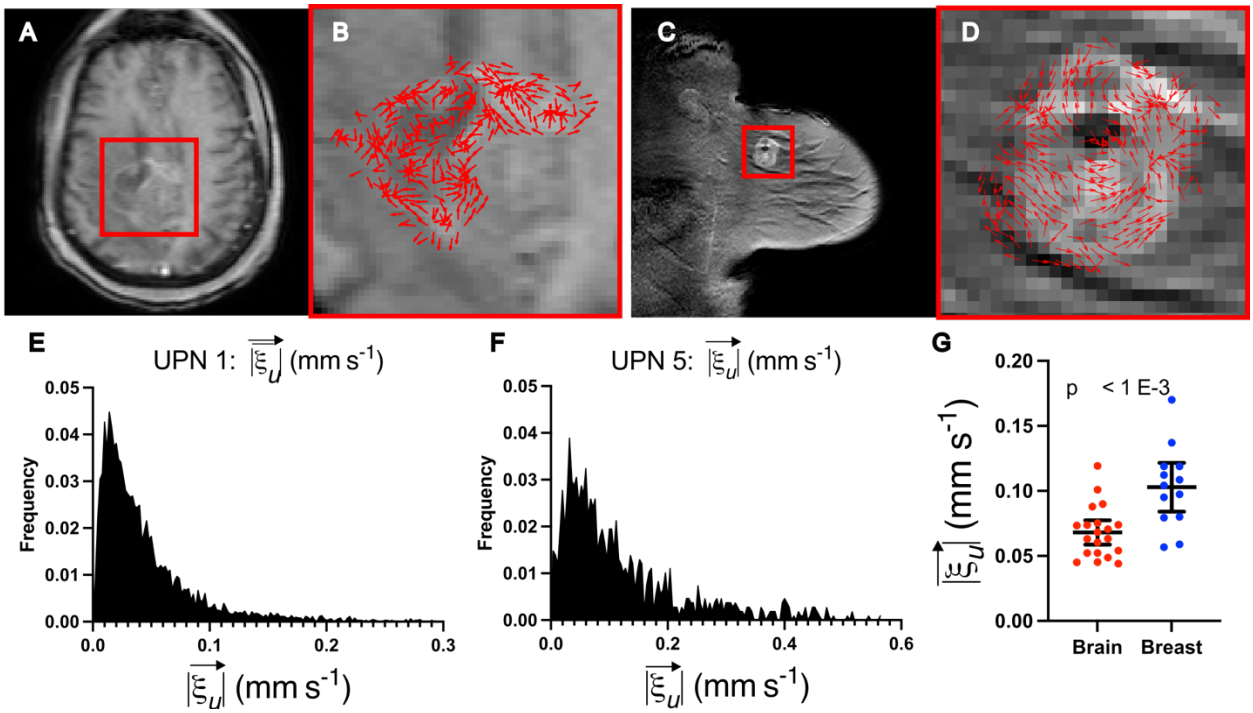

Figure 4: LCFR captures differences in fluid transport between breast and brain cancers. (A and B) Representative post-contrast T_1-weighted image of central slice of residual glioblastoma two weeks after resection surgery. (B) Detail of tumor and resection cavity, with overlay of the estimated velocity direction, $\vec{\xi_u}$. (C and D) Representative post-contrast T_1-weighted image of untreated primary breast cancer lesion. (D) Detail of the enhancing tumor, with overlay of the with overlay of the estimated velocity direction, $\vec{\xi_u}$. (E) Distribution of the in-plane velocity of the entire enhancing glioblastoma and resection cavity (mean = 5.23E-1 ± 5.10E-1). (F) Distribution of the in-plane velocity of the entire enhancing breast tumor (mean = 1.19E-1 ± 1.06E-1). (G) Mean fluid velocities for brain (mean = 6.81E-2 ± 1.99E-2 mm/s, N = 20) and breast data (mean = 1.03E-1 ± 3.10E-2, N = 13), with whiskers indicating mean and 95% confidence interval.

Supplementary Materials

Materials and Methods

In silico forward methods

Forward PDE models of advection, diffusion, and source of contrast in tissue are implemented using the 2-dimensional finite difference method on a 64 mm x 64 mm grid, with $\Delta x = \Delta y = 1\text{mm}$, with explicit time stepping. The boundary conditions are Dirichlet such that $(c(\vec{x}, t)_\Omega = 0)$.

Table S1: Description of in silico simulation parameters

Simulation	Diffusion Coefficient	Velocity Field	Source Dynamics	Explicit FDM dt
Divergent Flow	0.75 mm2/s	u_x = sqrt(2) sign(x) /2 mm/s u_y = sqrt(2) sign(y)/2 mm/s	None	1/8 s
Poiseuille Shear	0.75 mm2/s	$u_y = 0$ $u_x = 2.5\ (1-y)^2/32^2$	None	1/8 s
Extended Tofts-Kety	0	0	Ktrans (1/s): Q1 =0.1 Q2 = 0.2 Q3 = 0.4 Q4 = 1 v_e: 0.5 $v_p = 0.05$	1/16 min

Collagen-HA in vitro validation

Collagen hydrogels composed of 0.2% collagen (Corning) were crosslinked using 0.4% photo-crosslinkable HA for 45 seconds. Each in vitro phantom consists of 350uL of gel pipetted into a 12mm tissue culture insert (Millipore, Burlington, MA). Prior to imaging, 100uL of 1X PBS was applied below the gel, in a collection chamber. To induce flow through the gel, 300uL of a 1:100 dilution of Gd-DTPA (BioPal, Worcester, MA) in 1X PBS was administered atop the gel. The contrast front velocity was measured by calculating the number of pixels contrast traveled through the gel during the duration of MR imaging (Fig 2, A). Dynamic contrast enhancement imaging parameters match in vivo parameters (See Methods: Magnetic Resonance Imaging, 3D DCE). A single T10 map was acquired through VFA methods (See Methods: Magnetic Resonance Imaging, 3D DCE), across 3 replicates, and the mean T10 value within the gel was used for the T10 value across the 3 replicates to calculate the concentration of Gd-DTPA within the hydrogel.

Table S2: Location of contrast agent front selection

	Gel 1	Gel 2	Gel 3
[x,y,z,t] index of initial contrast front position	[46, 63, 6, 8]	[52, 62, 6, 7]	[49, 56, 6, 5]
[x,y,z,t] index of final contrast front position	[46, 70, 6, 48]	[52, 69, 6, 48]	[49, 62, 6, 48]

Description of in vivo animal studies

All animal procedures were reviewed and approved by the Institutional Animal Care and Use Committee in accordance with the NIH guidelines for animal research (Institutional Animal Care and Use Committee protocol number 20-146). Three month old, male C57Bl/6 mice (n=6, ~25g) were purchased from Charles River. The animals were housed in a room maintained at 20-23 °C, 45-55% relative humidity, and a 14-h/12-h light/dark cycle with access to standard laboratory chow and water until the experiment. Mice were injected with 100,000 green fluorescent protein (GFP)-expressing Gl261 (NCI-DTP Cat# Glioma 261, RRID:CVCL_Y003) cells in the cortex and allowed to grow for 14 days. No control group was used in this study as our primary outcome was to correlate flow and histological outcomes within a single animal. Following inoculation, mice were provided wet food and hydrogel for recovery, injected with 4mg/kg ketoprofen for 48 hours post inoculation, and weighed every other day for the duration of the study. Mice were allowed to live in group housing, with a max of four mice per cage. Mice were separated if wounds appeared indicating aggressive behavior.

Description of cell lines used

Lentivirus conferring expression of green fluorescent protein (GFP) under puromycin antibiotic selection was a generous gift from the laboratory of Dr. Kevin Janes. Murine GL261, which were originally derived using C57BL/6 male mice (NCI-DTP Cat# Glioma 261, RRID:CVCL_Y003) (*41*), were serially transduced with GFP lentivirus and purified by selection with 2 µg/mL puromycin (Thermo Fisher A1113803). Cells were maintained at 37 °C and 5.2% CO_2 for at least three passages after thaw with DMEM + 10% Fetal bovine serum (ThermoFisher, Gibco). Cells were resuspended at a concentration of 20,000 cells/uL in serum free media for tumor implantation. Our cell lines have not undergone cell authentication.

Preclinical magnetic resonance imaging

Following anesthesia, a catheter was inserted into the lateral tail vein. Mice were imaged with a 9.4T small animal MRI (Bruker, Ettingen, Germany) equipped with a 20mm RF surface coil. Two consecutive T2-weighted images were collected to verify tumor presence. The first image has high SNR to aid with MRI:IHC alignment for cryosectioning; the second T2-weighted image has

isometric voxels for registration to isotropic T1 images. T1 mapping was performed to collect baseline intensity, followed by a 3D DCE T1-weighted FLASH sequence. Six pre-contrast images were acquired before injecting gadolinium (0.2mL/kg, BioPal). A T1-weighted post-contrast image was acquired to confirm contrast enhancement. An extensive list of imaging parameters are included in **Table S1**. After completion of MRI, mice were injected with Evans Blue at a concentration of (1.6mL/kg) which was allowed to circulate overnight before tissue harvesting.

Table S3: Preclinical and hydrogel MRI imaging parameters

	1. T2-weighted	2. T2-Weighted	3. T1 mapping	4. T1-weighted DCE	5. T1-weighted
Sequence	RARE	RARE	RARE with varied TR	FLASH	FLASH
TE/TR	40ms/2600ms	40ms/2600ms	TE: 7ms TR: 5500, 3000, 1500, 800, 500, 300 ms	4ms/21ms	3ms/180ms
Number of Slices	16	12	12	1 (3D Imaging)	16
Slice Thickness	400 um	200 um	200 um	200 um	400 um
Rare Factor	8	8	2	n/a	n/a
Flip angle	90,180	90/180	90/180	25	70
FOV	19.2x19.2 mm	19.2 x 19.2 mm	19.2 x 19.2 mm	19.2 x 19.2 x 12 mm	19.2 x 19.2 mm
Matrix Size	192 x 192	96 x 96	96 x 96	96 x 96 x 12	192 x 192
Repetitions	1	1	1	48	1
Averages	9	18	18	1	7
Time of Acquisition	9 min 21 sec	9 min 21 sec	9 min 16 sec	24 min 11 sec	3 min 1 sec

Tissue harvest and immunohistochemistry

Mice were euthanized and transcardially perfused with 4% PFA and ice cold 1x PBS. Brains were post-fixed in PFA for 18 hours, and placed in 30% sucrose until complete submersion. Afterwards, brains were placed in molds of OCT at -80°C and sectioned at 12um on a cryostat. T2-weighted MRI images were used as a guide during sectioning to inform which MRI slice corresponded to the collected cryosectioned slice. Structural features (i.e ventricles, white matter, tumor shape) were used as visual aides to confirm location, and compared to the corresponding sagittal MRI slice. Brain sections were stained for DAPI (ThermoFisher) and imaged at 20X on an VS200 Olympus Slide Scanner (Olympus).

Immunohistochemistry comparison to MRI

To visually compare MRI to histology, all IHC stains were first loaded into MATLAB, and then down-sampled to 0.2 mm in-plane resolution to match the resolution of isotropic MRI. This down-sampling was done using the *blockproc* function in MATLAB, summing the total intensity of sub-pixels within the larger super-pixels so as to maintain the total image intensity. A ROI

was drawn around the tumor region of the DAPI stain, using the *drawfreehand* function in MATLAB, as well as on the corresponding slice of post-contrast DCE-MRI.

Immunohistochemistry Evans Blue coverage calculation

Evans Blue stains from individual animals were processed using FIJI image processing software to calculate percent tumor coverage. First, a threshold was applied, removing the lower 95th percentile of the image intensity. A mask of the tumor was draw on the DAPI stain to demarcate the tumor using FIJI's "mask" functionality. This mask was then applied to the Evans Blue stain, and the percent of voxels greater than the 95th percentile intensity within the tumor ROI was reported. The percent tumor Evans Blue coverage was then taken and compared to the mean tumor intensity value of ξ_{trans} on an individual animal basis, and the correlation and significance of the correlation was determined using a Pearson correlation test.

Clinical imaging: QIN BREAST-02

The study of publicly available data and was approved by the local Institutional Review Board Protocol 15286. All 13 patients from the QIN BREAST-02 dataset, provided by The Cancer Imaging Archive (TCIA), were analyzed using LCFR. All patients (female, 18+) were diagnosed with invasive breast cancer, with lesion size > 1cm. Images used were while all patients were treatment-naïve, though all patients received treatment after initial imaging. The multi-flip T1 map and DCE sequences, acquired on Phillips 3T scanners located at both Vanderbilt University Medical Center, and University of Chicago, were used in this study (*33*). Image acquisition details can be found on the TCIA website for the BREAST-02 study.

Clinical imaging: Glioblastoma patients

The retrospective study of City of Hope patient data was approved by the local Institutional Review Board Protocol 15286. 20 patients who came to City of Hope National Cancer Center in Duarte, CA, for advanced imaging after resection of glioblastoma between January 2020, and July 2022, with residual enhancing lesion size > 1cm underwent DCE-MRI. Patients underwent imaging between 3 and 135 days post-resection (mean = 32.3, median 28, SD = 30.7). Scans were performed on a 3T Siemens scanner. The DCE scan consisted of 3D FLASH sequence with prior variable-flip angle T1-mapping. Variable Flip angles were acquired at 2,5, and 10 degrees, repetition time = 9.3 ms, and echo time of 4.29 ms. The dynamic scan was performed with 50 phases at 6 second temporal resolution, flip angle = 15 degrees, repetition time = 9.3 ms, and echo time of 4.29 ms. 8 mL of Gadovist (Bayer, Whippany, NJ) was administered during the sequence. The size of the imaging FOV was 192 x 132 in-plane (1.46 mm resolution), and 16 slices with 5 mm slice thickness, identical between the dynamic scan and variable flip angle scans.

Table S4: GBM patient age and sex

Unique Patient Identifier (UPN)	Patient age at imaging (years)	Patient sex
1	58	F

2	47	F
3	47	F
4	52	M
5	42	M
6	60	M
7	54	M
8	38	F
9	40	F
10	36	M
13	19	M
14	71	M
15	57	F
16	28	M
17	40	F
18	59	F
19	55	M
20	69	F
21	34	F
22	37	M

Statistical testing

All statistical analyses and tests were performed using GraphPad Prism 9 (GraphPad Software, San Diego, CA).

DCE-MRI pre-processing

Each of the variable flip angle images and dynamic T1-weighted images are rigidly registered to the first dynamic T_1 image. From images acquired using variable flip angles, α, a T_{10} map for each individual was is calculated by regression (*42*):

(S1) $S(t) = S_0 \frac{\left(1-exp\left(-\frac{T_R}{T_{10}(t)}\right)\right)sin\,(\alpha)}{1-cos(\alpha)\,exp\left(-\frac{T_R}{T_{10}(t)}\right)}$

Where S is the measured signal intensity, S_0 is baseline non-contrast-enhanced signal intensity, TR is the repetition time, T_{10} is the native T_1 relaxation time of the tissue, and α is the flip angle.

From the calculated T_{10} map (*43*), and the relaxivity (r_1) of the contrast agent (Gadovist, $3.7s^{-1}mM^{-1}$ for 3T, and $3.3\ 7s^{-1}mM^{-1}$for 7T (*44*)), the sequential T_1-weighted images are converted into a spatiotemporal map of contrast agent concentration (*45*) by

(S2) $R_1 = r_1 C_t(t) + R_{10}, R_1 = \frac{1}{T_1}$

(S3) $\frac{1}{T_1(t)} = \frac{1}{T_{10}} + r_1 C_t$

Where R_1 is the inverse of the T_1-relaxation time, and R_{10} is the baseline relaxation, or the inverse of the baseline T_{10} relaxation time.

After calculation of contrast agent concentration, the local contrast bolus arrival time (BAT) is calculated by bilinear regression (*46*). Briefly, a sub-set of each individual voxel's time-enhancement curve, c_{sample}, is considered, from the initial time point to the time point with maximal concentration of contrast agent. The points 0, and t_f correspond to the initial and final timepoints, and the point p_1 corresponds to a time points BAT ϵ (0, t_f). The BAT is determined to be the value that minimizes the summed square error between the bilinear fit and the data

(S4) BAT = $argmin_{BAT}\left(\Sigma\left(f(i,\text{BAT}) - c_{sample,i}\right)^2\right)$

(S5) $f(i,\text{BAT}) = \begin{cases} m_1 t + b_1, t \leq BAT \\ m_2 t + m_1 BAT, i > BAT \end{cases}$

An empirical vascular input function (VIF) is then measured using the automatic-VIF selection algorithm detailed by Singh et al. (*47*). Briefly, this method selects voxels which are rapidly enhancing (BAT < 10s), and enhance within the upper 90th percentile of all voxels. The signal intensity is then normalized and scaled to account for partial volume effect and hematocrit. This method is utilized for the CoH GBM patients, the QIN BREAST-02 dataset, and in vivo mouse model. The individual-specific VIF is adjusted for each individual voxel such that the BAT for the VIF matches the estimated BAT of the individual voxel's enhancement time course, using S4-S5.

Weak SINDy for PDEs

Model identification and inversion was performed as follows. Briefly, SINDy identifies dynamics through sparse regression, with the assumption that the time-derivative of the state-space data is a linear combination of polynomial terms of all measured state-space data, and their corresponding spatial and temporal derivatives (*28*):

(S6) $\frac{\partial}{\partial t} Y = f(Y)$

where Y is the measured state-space data. f is a library consisting of linear combinations of analytic functions of Y. In our case, *c*, for contrast agent, is the measured state-variable. In this work, subscript notation is utilized as follows: $Y_q = \frac{\partial}{\partial q} Y$, $Y_{qq} = \frac{\partial^2}{\partial q^2} Y$. Typically, f consists of the measured state-space data itself, it's spatial and temporal derivatives, and polynomial combinations of these measurements and their derivatives:

(S7) $f(c) = \Theta(c)\Xi$

(S8) $\Theta(c) = [1, c, c^2, \dots, c_x, c_{xx}, \dots]$

(S9) $\Xi = \left[\xi_1, \xi_2, \xi_3, \dots, \xi_Q\right]^T$

As DCE-MRI is typically modeled as exchange between plasma and extravascular, extra cellular (EES) interstitial space, a BAT-adjusted VIF term and its first derivative are included in the library (*48*). In previous literature, Tofts and Kety parameterized local contrast agent dynamics as

(S10) $\frac{\partial c}{\partial t} = K^{trans}(X)VIF(X,t) - K^{ep}(X)c(X,t) + v_p(X)\frac{\partial VIF(X,t)}{\partial t}$

Where, c(X,t) is the contrast agent concentration, K^{trans} is the volumetric flux per unit tissue volume of contrast from vasculature to tissue, K^{ep} is the volumetric return flux per unit tissue volume from tissue to contrast, and v_p is the contrast concentration within the plasma compartment, which does not extravasate into the tissue. A practical guide to acquisition of DCE data and its application to this model may be found from Barnes et al. 2012 (*45*). Each of the above terms are included in the function library Θ.

As the VIF may be considered an empirically determined forcing or source function, it is important to include this in the function library. The coefficient in front of the VIF term is mathematically comparable to K^{trans}, whereas the coefficient in front of the measured concentration is comparable to K^{ep}. Due to potentially high plasma content in high-grade gliomas and other cancers, there may be significant signal contribution from contrast agent within blood plasma. As such, the first temporal derivative of the VIF is also included in the library. The coefficient in front of this term is typically referred to as v_p in a Tofts-Kety framework.

The full function library Θ consists of all terms in the Tofts-Kety model extended by advection and diffusion:

(S11) $\frac{\partial c}{\partial t} = \nabla \cdot D\nabla c - \nabla(\vec{u} \cdot c) + R,$

where,

(S12) $R = K^{trans}VIF(t) - k_{ep}c + v_p \frac{\partial VIF}{\partial t},$

Where D is the diffusion coefficient, and $\vec{u}$ is the contrast agent velocity.

The PDE may be expanded to reveal terms as follows:

(S13) $\frac{\partial c}{\partial t} = (\nabla D) \cdot (\nabla c) + D\nabla^2 c - c\nabla \cdot \vec{u} - \overrightarrow{u} \cdot \nabla c \ + K^{trans}\, VIF(t) - k_{ep}c + v_p \frac{\partial VIF}{\partial t},$

and factored by partial derivatives of terms c(X,t) and VIF(X,t):

(S14) $\frac{\partial c}{\partial t} = D\nabla^2 c + (\nabla D - \vec{u}) \cdot (\nabla c) + \left(-k_{ep} - \nabla \cdot \vec{u}\right)c + K^{trans}VIF(t) + v_p \frac{\partial VIF}{\partial t}.$

This form of the system may be put in the SINDy framework (S6-S9). Thus, the linear model regression problem takes the form:

(S15) $f(Y) = \frac{\partial c}{\partial t} = \overline{\xi_D}\nabla^2 c + \overrightarrow{\xi_u} \cdot (\nabla \cdot c) - \xi_{ep}c + \xi_{trans}VIF(t) + \xi_{VIF}\frac{\partial VIF}{\partial t} = \Theta(c, VIF)\Xi$

It is assumed that the diffusion is isotropic such that:

S(16) $\xi_{\overline{D}} = \left(\xi_{D,x} + \xi_{D,y} + \xi_{D,z}\right)/3$, for the 3D case, and $\xi_{\overline{D}} = \left(\xi_{D,x} + \xi_{D,y}\right)/2$, for the 2D case

and similarly for the velocity field,

S(17) $\overrightarrow{\xi_u} = \left(\xi_{u,x} \cdot \hat{\imath} + \xi_{u,y} \cdot \hat{\jmath} + \xi_{u,z} \cdot \hat{k}\right)$

Where $\hat{\imath}, \hat{\jmath}, \hat{k}$ are the standard unit vectors in the (x, y, z) directions, respectively.

We do not attempt to separate the contribution to regression coefficients from multiple contributing PDE terms, as they are analytically unidentifiable without estimating the spatial gradient of the diffusivity field D, without using further weak derivatives. As such, we present our results in terms of the regression coefficients ξ from the function library, agnostic of the structure of the underlying PDE.

The 3D or 4D data matrix of local, time-resolved concentration of contrast agent, c(x,y,z,t), is acquired either through simulation, or measurement via MRI. MRI data is often noisy in both space and time and may have varying resolutions. To efficiently and accurately perform the regression, rather than utilizing a finite-difference approach for estimating the spatial and temporal derivatives of the measured data, a weak derivative approach is taken to smooth the data. Additional details of the weak PDE regression methodology may be found in Messenger & Bortz (*30*). First, the inner product of (S7) and a given basis function Ψ is taken over the entire spatiotemporal domain on both sides of the equation:

(S18) $< \Psi, f(c) >_{t,\Omega} = < \Psi, \Theta(c)\Xi >_{t,\Omega} = \Sigma_{q=1}^{Q} < \Psi, \xi_q \theta_q >_{t,\Omega}$

We take the basis functions Ψ to be a tensor product of 1-dimensional polynomial approximations of a 4D Gaussian curve, of the family:

(S19) $\psi^{x}(m) = \begin{cases} C(m-a)^6(b-m)^6, a < m < b \\ 0 \; otherwise \end{cases}$

The span of the basis functions [a,b] (in real space/time units (off-grid)) in each dimension is selected using the critical wavelength analysis provided by Messenger and Bortz, 2021. In each dimension, ψ is normalized by selection of coefficient *C*, such that

(S20) $C \int_a^b \psi(m) dm = 1.$

This family of basis functions was selected as it serves to smooth the data as a polynomial approximation to a Gaussian, has analytical expressions for derivatives, and is equal to 0 at the boundary for each of the derivatives required for the construction of the library (for our use case, derivatives up to order 4). Integration by parts is performed on each term in the library, and on the left hand side of the partial differential equation, until the remaining analytic weak derivative form of each term requires no derivatives on the raw data. This methodology effectively transfers the derivatives from the noisy data onto smooth basis functions, while preserving the PDE coefficient in the weights vector Ξ. This is demonstrated in one-dimension as:

(S21) $\int_a^b \psi^{x} c' dx = [\psi^{x} c]|_a^b - \int_a^b \psi^{x\prime} c \; dx$

(S22) $\int_a^b \psi^{x} c' \; dx = - \int_a^b \psi^{x\prime} c \; dx$

Note that the boundary term vanishes on the boundaries. Practically, Eq S22. is performed using convolution of data *c*, and basis function Ψ or its derivatives. It is assumed that *w* is spatially invariant on a 3x3x3 sample grid of MR data, and over all time, thus, allowing for the weight *w* to be factored from the matrix equation. The vector of weights, Ξ_n, is solved for in parallel using L2 regression on each of the *N* unique 3x3x3 windows of the data matrix, for all time. In the original implementation of SINDy, L1 or SR3 regression is used to enforce sparsity (*28*). This implementation often involves a parameter sweep and selection of an appropriate sparsity-enforcing parameter through Pareto Front analysis (*40*). However, due to the large number of regressions which need to be performed for spatially localized parameterization, the authors opt for L2 regression, avoiding the problem of spatially localized hyperparameter tuning. For each window *n*, the weights $\xi_{q,n}$ of each weak derivative are calculated:

(S23) $- \int_0^{t_f} \int_\Omega \Psi_t c(x,y,z,t) dt d\Omega \; = \sum_{q=1}^{Q} \int_0^{t_f} \int_\Omega \xi_{q,n} \Psi_q c(x,y,z,t) dt d\Omega$

(S24) $\ldots = \sum_{q=1}^{Q} \xi_{q,n} \int_0^{t_f} \int_\Omega \Psi_q c(x,y,z,t) dt d\Omega$

On each individual sliding window n, we have

(S25) $\widetilde{c_{t,n}} = \Xi_n \tilde{\Theta}^T(c)_n = \tilde{\Theta}(c)_n \Xi_n$

where $\widetilde{c_{t_n}}$ is the weak time-derivative of the measured signal enhancement curve within the window, Ξ_n is a vector containing the weights $\xi_{q,n}$, and $\widetilde{\Theta}(x)_n$ is the library containing all corresponding weak spatial and temporal derivatives of the data for sliding window n of N, where N is the total number of sliding windows. This system is solved using L_2 norm, so as to avoid solving for a localized sparsity enforcing parameter required using the L1, LASSO, or SR3 methodologies:

(S26) $J_n = \left(\|\widetilde{c_{t_n}} - \tilde{\Theta}(c)_n \Xi_n\|_2\right)$

Pseudo-code for the entire localized convolutional function regression algorithm may be found below:

Pseudo-code

1. Initialize $c(x, y, z, t)$
2. Select region of interest for VIF, or apply automated VIF selection
3. For each voxel:
    a. Adjust the VIF BAT to match the voxel BAT
4. Assemble library of polynomial terms present in transport equation S15
5. Perform critical wavenumber analysis for each dimension to select the span and shape of the basis functions $\psi^x, \psi^y, \psi^z, \psi^t$
6. For each dimension, calculate ψ and it's partial derivatives
7. Calculate $\Psi(x, y, z, t) = \psi^x \otimes \psi^y \otimes \psi^z \otimes \psi^t$, and all required tensor product combinations for each weak derivative.
8. For each library member, calculate the weak derivative of the data:
    a. $\theta_q = -< c(x, y, z, t), \Psi_q >_{t,\Omega}$
9. Calculate the left-hand side $\widetilde{c_t} = < c(x, y, z, t), \partial_t \Psi >_{t,\Omega}$
10. Subdivide the image into N overlapping 3x3x3 windows
11. For each window, n of N:
    a. Solve the local convolutional function regression using L2 regression for window n.
12. For each library term, q of Q:
    a. Overlay heat map of ξ_q on post-contrast MR image

Note, that the above pseudo-code is specific to 3 spatial dimensions. This 3-D implementation was utilized for MRI data consisting of isotropic spatial resolution. An equivalent algorithm was

utilized in 2D for data where the z-slice thickness was greater than the in-plane voxel resolution and applied on each individual slice instead of to the entire volume.

The algorithm for this implementation of LCFR is performed in MATLAB 2022b, including the Image and Signal Processing Toolboxes (Natick, MA).

Supplementary Results

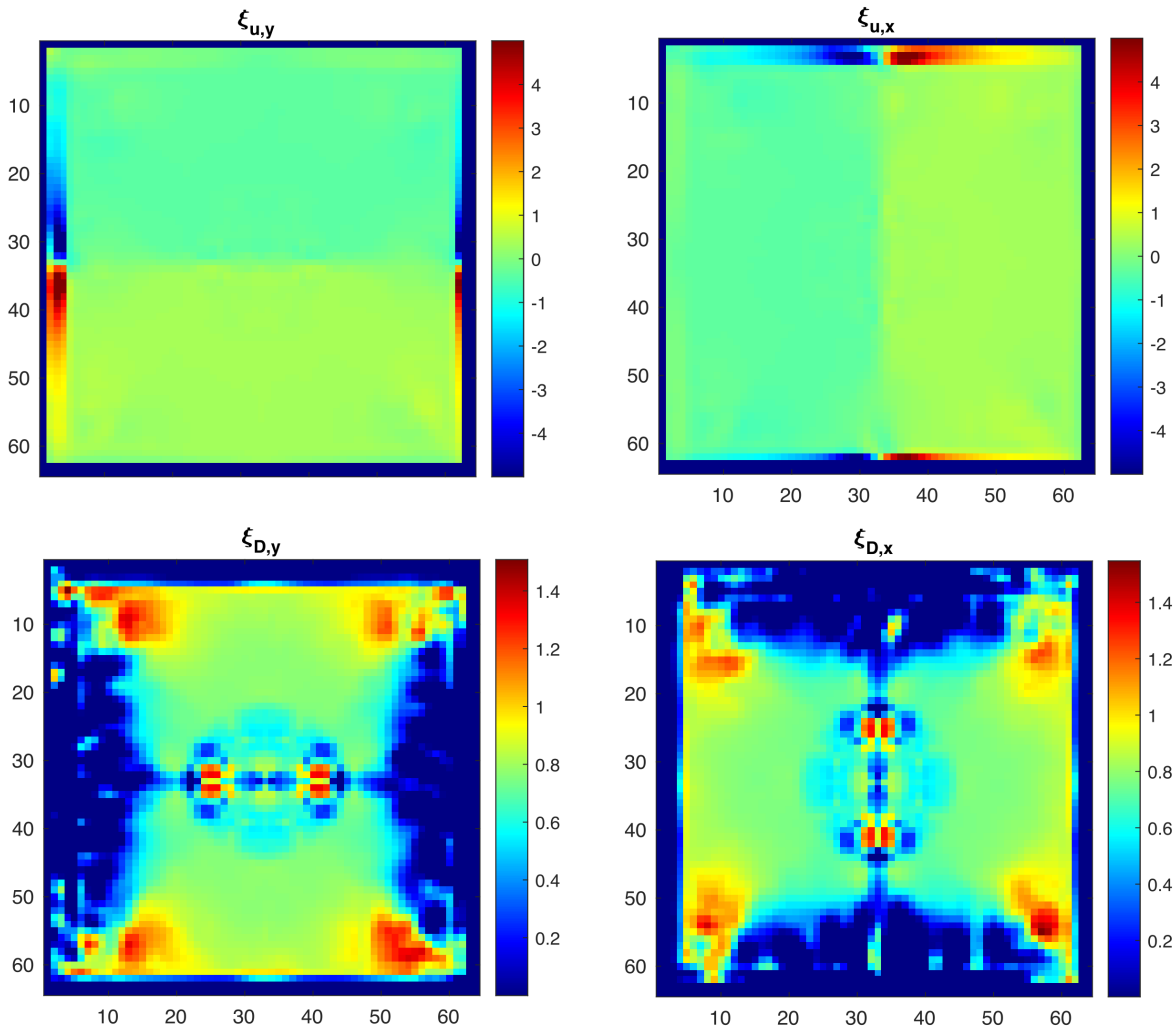

Supplemental figure 1. Raw output of outward flow validation. Boundary effects are due to the Gibbs phenomenon resulting from the use of the Fourier transform to perform the convolution of the concentration with the basis functions. Advection accuracy is accurate in regions of strong signal. $\xi_{\bar{D}}$ accuracy is also accurate but is more susceptible to edge effects than $\overrightarrow{\xi_u}$.

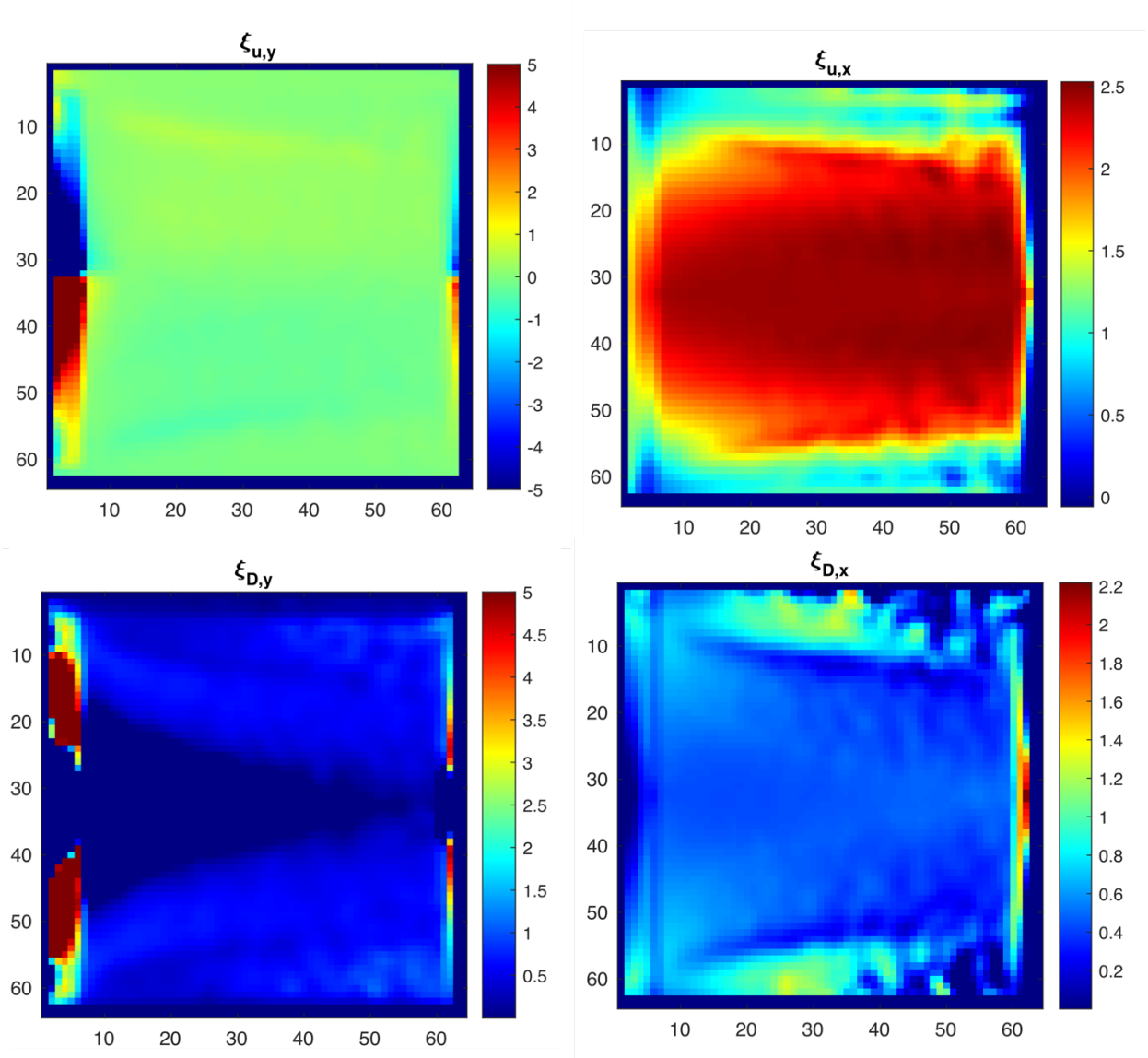

Supplemental figure 2. Raw output of shear flow validation. Similar to the outward flow simulation, edge effects are due to the convolution of the concentration with the basis functions and are the result of the Gibbs phenomenon. Edge effects are strongest at initial conditions and boundaries. Accuracy is highest in regions furthest from boundaries, and where contrast was present in high quantities.

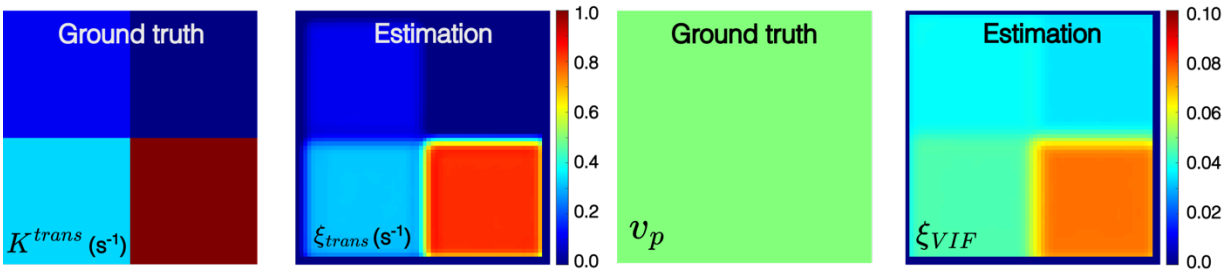

Supplemental figure 3. Validation on Tofts-Kety perfusion phantom, where K^{trans} is varied by quadrant, and v_p is held constant. See Supplemental Table 1 for simulation parameters. LCFR accurately estimates the contrast perfusion rate, K^{trans}, and v_p is accurately estimated, though biased by Ktrans signal. This is largely because v_p and K^{trans} are often practically non-identifiable.

Technical Considerations

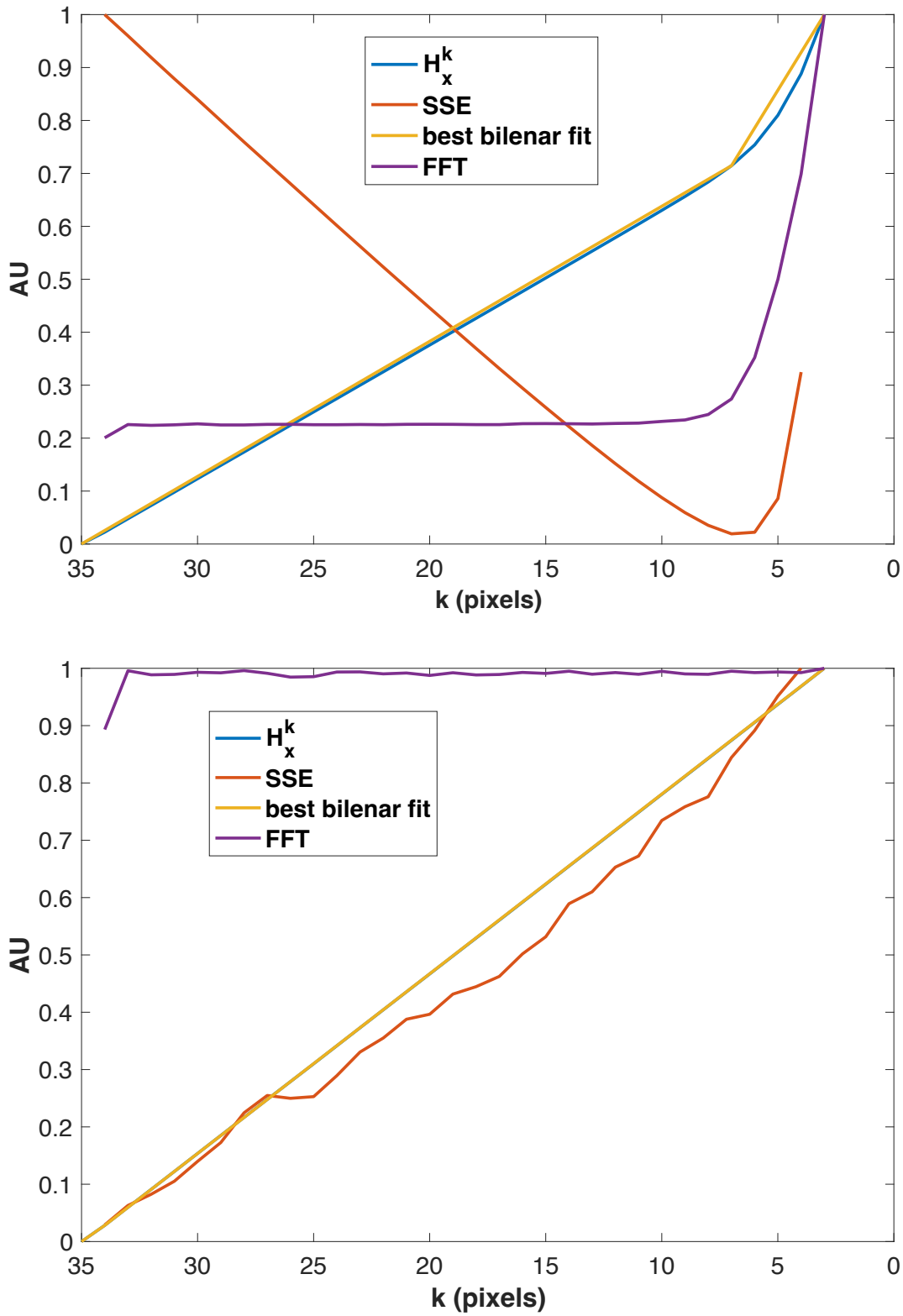

Supplemental figure 4. **Basis function selection criteria.** a) Selection of k* (x-direction) from in silico model of Laminar *Poiseuille* flow, with 1% Gaussian noise added. Note the clear global

minimum of the SSE of the bilinear fit selected for k*. b) Identical analysis performed on data with 50% noise added. Note the lack of distinct global minimum in SSE of the bilinear fit. The variance of the Gaussian noise is calculated as $\sigma^2 = f\max(Gd(X,t))$, where $f \epsilon (0,1]$, or $f \epsilon (0\%, 100\%]$ in percent of maximum signal. In Figure 1 (main text), 0.1% noise is added to stabilize the methodology, as the automatic basis function selection algorithm is designed with the expectation of system noise to filter.

Basis-function selection

Weak SINDy requires selection of basis functions to smoothly represent discrete data. To automatically select appropriate basis functions, a critical wavenumber, k*, is chosen for each spatial and temporal dimension. This selection is performed with the Fast Fourier Transform of the data in each dimension. Then, the cumulative sum of the FFT, H_q^k (where q is a dimension *x,y,z*, or *t*) is calculated, and approximated by bilinear-fit $b(k)$,

(S27) $$b(k) = \begin{cases} m_1 k, \ k > k^* \\ m_2 k + m_1 k^*, \ k \leq k^* \end{cases}$$

where k* is the critical wavenumber which minimizes the SSE between $b(k)$ and H_q^k. A basis function, in the form of a polynomial low-pass filter (Supplemental Equation 19), is selected such that frequencies greater than k^* are filtered out by a factor of 10^{-9} upon convolution of the function with the data. The factor of 10^{-9} was selected empirically, as it provides a balance between noise filtration and minimizing the span of the basis function.

This methodology is useful for MRI data, as it enables the filtering of noise introduced during image acquisition. However, the FFT approach carries with it two primary limitations. First, high frequencies are filtered out from analysis because the resolution of the basis-functions are necessarily lower than the resolution of the image, meaning fine-scale features of the dynamics are filtered and removed from analysis. Second, this method cannot work with data which are too sparse to represent with smooth functions. This second limitation means that weak SINDy cannot be faithfully applied to data which is has fewer samples ($n_{samples,d}$) less than the polynomial order chosen ($n_{samples,d} < p - 1$, where p is the polynomial order), or where the SSE of the bilinear fit of H_d^k does not have a distinct global minimum. In practice, we have found that this theoretical limitation is insufficient, and that roughly $2p$ datapoints are required. We only present the use of this methodology in cases where there is a distinct separation between signal and noise (through critical wavenumber k^* calculation), and where there are sufficient dimensional samples to be accurately represented by a 6th order polynomial. When the z-slice thickness is more than 2x the in-plane resolution, the 2D method is performed on each individual slice. This 2D methodology may also be applied when the number of z-slices is less than 12 (when using 6th order polynomials).

Convolutional implementation considerations

Further limitations arise from edge effects due to Gibbs phenomenon at edges, after convolution of the data with the basis functions. Convolution is performed practically using multiplication in k-space after performing an FFT on the data and basis function. These effects are first mitigated by padding with the edge-values using the *padarray* function in MATLAB (Natick, MA), with the 'replicate' option set to 'both'. Second, edge values are removed from the results where Gibbs phenomenon are most prominent.

Model assumptions and applicability

This methodology is built on the assumption that contrast agent is present in the tumor interstitium in sufficient quantities to be detected by MR. This assumption only holds for regions where there is sufficient blood supply or leaky vasculature to supply the tissue with contrast agent. As such, the resulting function regression does not correlate strongly with the data in regions with low concentration of contrast agent leakage. Masks were drawn to only including tumor tissue, and to avoiding healthy tissue and vasculature, so as to not bias the numerical analysis towards regions where the model assumptions do not apply.

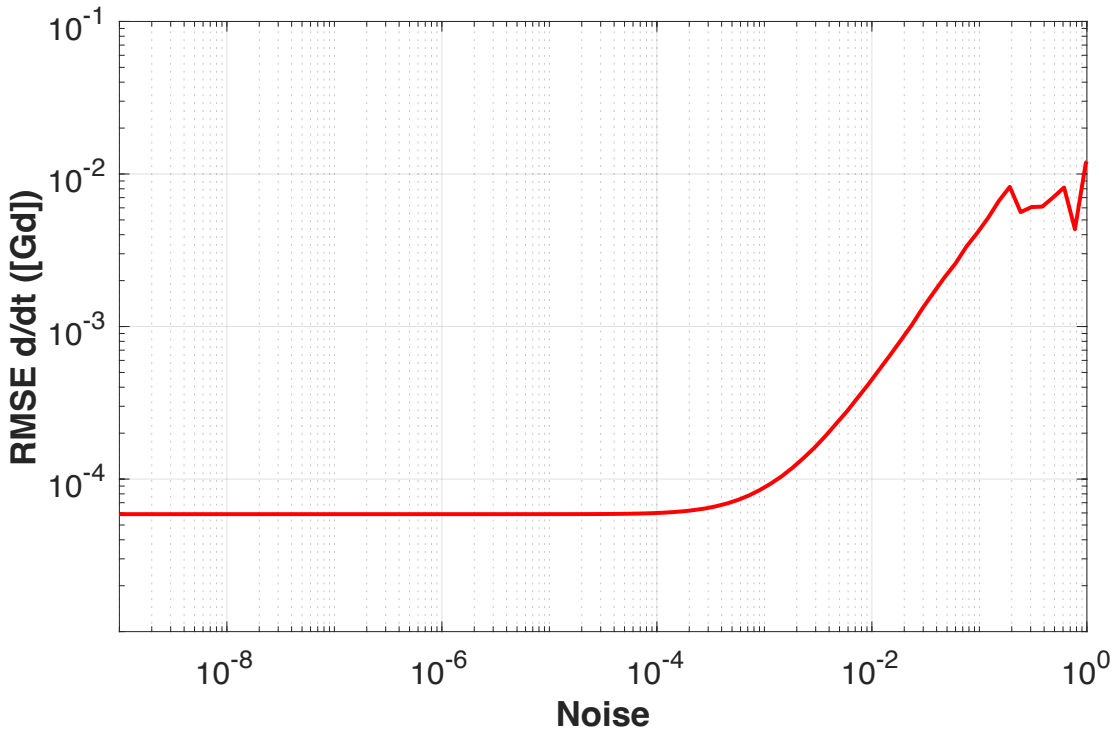

Supplemental figure 5. **Regression error vs. added Gaussian noise for in silico *Poiseuille* flow.** Root mean square error (RMSE) is the regression reconstruction error with respect to the observed weak time-derivative, and the variance of the noise is calculated as $\sigma^2 = f \max([Gd(X,t)])$, where $f \epsilon (0,1]$. The RMSE converges to a minimum at approximately $f < 1E-3$, and the reconstruction loses coherence with the original observations at approximately $f > 1E-1$. Our method of weak function regression is robust to noise up to roughly 10% of the maximum signal measured.

Limitations due to T_{10}-mapping

Model discovery techniques rely on the assumption that the state variable measured is the same variable which is being modeled. The objective of this methodology is to estimate the transport parameters of interstitial fluid, thus the present methodology relies on accurate quantitation of spatiotemporally resolved Gadolinium concentration. As such, we cannot rely on raw MR signal intensity measurements alone. In T_1-weighted MRI, the T_1 relaxation time is a non-linear function of contrast agent concentration, c:

(S28) $c = \frac{1}{r_1}\left(\frac{1}{T_1} - \frac{1}{T_{10}}\right)$,

where r_1 is the contrast agent relaxivity, T_1 is the T_1 relaxation time upon interaction with the contrast agent, and T_{10} is the native tissue T_1 relaxation time without the presence of contrast agent. As such, a T_{10} map must be acquired prior to contrast injection, typically through the variable flip angle (VFA) method or variable TR (VTR) method (*49*). This allows for the measured T_1-weighted signal intensity to be corrected for T_{10} inhomogeneity of the tissue, and the true concentration to

be estimated in space and time. In this work, we present imaging results only where a T_{10} map was acquired correctly. In some cases, it has been shown that a singular literature T_{10} value may be used to estimate contrast agent concentration (*50*). While this practice may be admissible in practice for ODEs parameter estimation of contrast agent transport, it results in spurious spatial concentration gradients required for PDEs parameter estimation. This effect can be seen in the QIN Prostate dataset, where a literature T_{10} value of 1600 ms was used. **Figure S5** depicts the predicted direction of the vector $\overrightarrow{\xi_u}$, clearly demonstrating a strong dependence on strong gradients in the image.

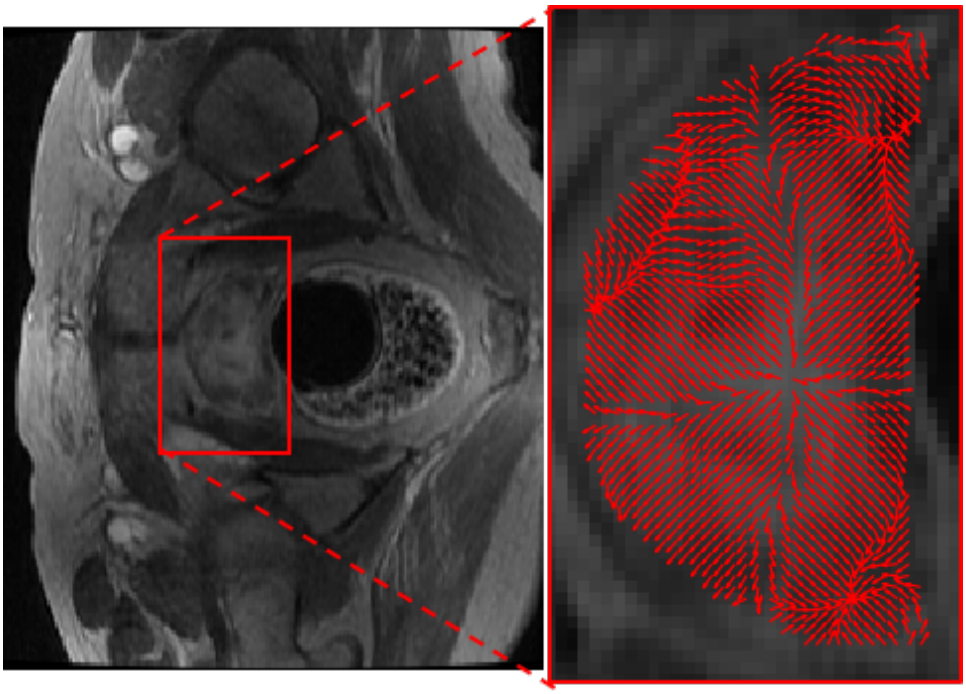

Supplemental figure 6: **Demonstration of technique on dataset without T10-map.** The direction of $\overrightarrow{\xi_u}$ strongly correlates with anatomical gradients along the capsule of the prostate, due to inability to calculate the T10 map directly from a properly-acquired VFA MRI sequence. This dataset was acquired with variable flip angles, but the flip angle scan also had varying repetition time, leading to an inability to calculate a proper T1-map, forcing a literature value to be used. As such, this data was not included in the analysis. All other figures shown in this work utilize a VFA- or VTR- acquired T_{10} map to calculate the proper concentration, preventing the occurrence of spurious image gradients due to variations in native T_{10} from the analysis.

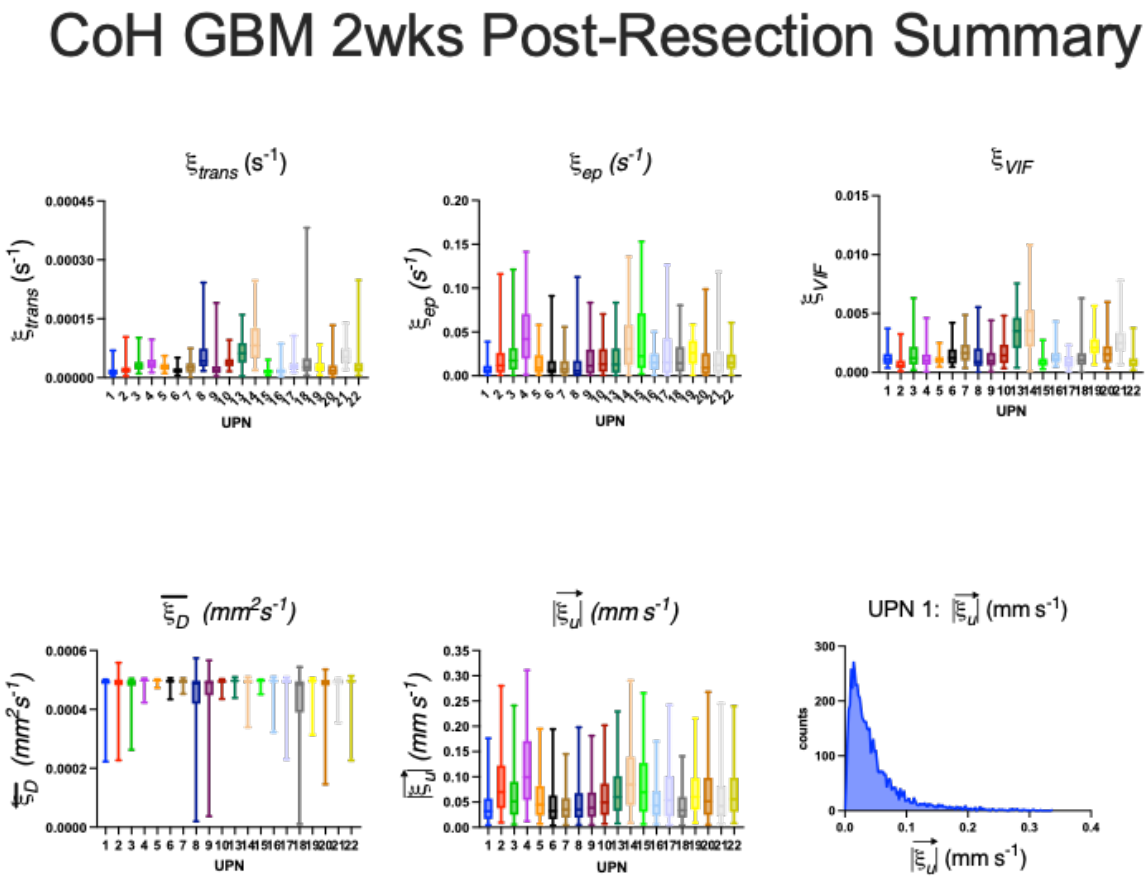

Supplemental figure 7: Summary of LCFR coefficients in the CoH GBM Cohort. The in-plane resolution of the voxels was 1.46 mm, and the slice-thickness was 5 mm. As the slice thickness was more than 2 times the in-plane resolution, the method was applied in 2 dimensions, neglecting the z-component of velocity- and diffusion- associated parameters. The results shown here, and in the tables, below are the results of analysis over a hand-drawn mask, and the logical intersection where the R^2 value of the method with respect to the weak-time derivative of the data is $R^2 > 0.5$.

Table S5: CoH GBM Cohort Summary, Parameter Means

UPN	$\lvert\overrightarrow{\xi_u}\rvert$ (mm/s)	$\overline{\xi_D}$ (mm^2/s)	ξ_{VIF} (frac.)	ξ_{ep} (s^{-1})	ξ_{trans} (s^{-1})
1	4.52 E-2	4.76 E-4	1.32E-3	9.27 E-3	1.82 E-5
2	8.99 E-2	4.78 E-4	8.584 E-4	2.40 E-2	2.46 E-5
3	6.83 E-2	4.73 E-4	1.74 E-3	2.51 E-2	3.55e E-5
4	1.19 E-1	4.93 E-4	1.29 E-3	5.15 E-2	3.87e E-5
5	6.04 E-2	4.95 E-4	1.13 E-3	1.62 E-2	2.85e E-5
6	4.88 E-2	4.904 E-4	1.50 E-3	1.57 E-2	2.02e E-5
7	4.41 E-2	4.92 E-4	1.85 E-3	1.25 E-2	2.70e E-5
8	5.23 E-2	4.29 E-4	1.53 E-3	1.61 E-2	6.47e E-5
9	5.23 E-2	4.44 E-4	1.31 E-3	2.03 E-2	3.28 E-5
10	6.30 E-2	4.90 E-4	1.79 E-3	2.05 E-2	4.11 E-5
13	7.52 E-2	4.92 E-4	3.51 E-3	2.13 E-2	6.70 E-5
14	1.01 E-1	4.84 E-4	4.00 E-3	3.93 E-2	9.60 E-5
15	8.80 E-2	4.92 E-4	9.76 E-4	4.35 E-2	1.75 E-5
16	5.41 E-2	4.84 E-4	1.43 E-3	1.78 E-2	2.03 E-5
17	7.06 E-2	4.79 E-4	9.53 E-4	2.78 E-2	3.45 E-5
18	4.51 E-2	4.14 E-4	1.47 E-3	2.20 E-2	6.05 E-5
19	7.38 E-2	4.81 E-4	2.34 E-3	2.66 E-2	3.04 E-5
20	7.35 E-2	4.68 E-4	1.94 E-3	1.97 E-2	2.94 E-5
21	6.32 E-2	4.83 E-4	2.86 E-3	2.17 E-2	5.95 E-5
22	7.40 E-2	4.79 E-4	1.05 E-3	1.85 E-2	4.41 E-5
Mean	6.81E-2	4.76 E-4	1.741 E-3	2.35 E-2	3.95 E-5

Table S6: CoH GBM Cohort Summary, Parameter 95% CIs

UPN	$\lvert\overrightarrow{\xi_u}\rvert$ (mm/s)	$\overline{\xi_D}$ (mm^2/s)	ξ_{VIF} (frac.)	ξ_{ep} (s^{-1})	ξ_{trans} (s^{-1})
1	4.41E-3	6.98E-5	1.01E-3	1.02E-2	1.89E-5
2	7.18E-2	7.95E-5	8.62E-4	4.47E-2	2.79E-5
3	6.13E-2	6.32E-5	1.79E-3	2.89E-2	2.99E-5
4	8.41E-2	2.60E-5	1.06E-3	4.15E-2	2.26E-5
5	5.09E-2	2.19E-5	5.29E-4	1.66E-2	1.32E-5
6	4.95E-2	3.15E-5	1.01E-3	2.43E-2	1.48E-5
7	3.60E-2	1.93E-5	1.19E-3	1.47E-2	1.89E-5
8	5.10E-2	1.42E-4	1.89E-3	2.67E-2	6.61E-5
9	4.56E-2	1.23E-4	1.25E-3	2.34E-2	5.44E-5
10	5.19E-2	2.59E-5	1.26E-3	2.03E-2	2.02E-5
13	5.86E-2	2.81E-5	2.04E-3	2.36E-2	4.09E-5
14	7.39E-2	5.80E-5	3.45E-3	3.50E-2	6.50E-5
15	7.12E-2	3.20E-5	7.42E-4	4.69E-2	1.16E-5
16	4.38E-2	5.47E-5	9.87E-4	1.44E-2	2.17E-5
17	6.27E-2	6.92E-5	6.09E-4	3.28E-2	3.42E-5
18	3.81E-2	1.49E-4	1.62E-3	2.33E-2	1.04E-4
19	5.48E-2	5.91E-5	1.19E-3	1.70E-2	2.73E-5
20	6.84E-2	9.38E-5	2.27E-3	2.64E-2	5.67E-5
21	6.02E-2	4.80e-5	1.84E-3	2.78E-2	3.12E-5
22	6.13E-2	7.68e-5	9.32E-4	1.57E-2	9.9E-5
SD of Patient Mean	1.99E-2	2.19E-5	8.45E-4	1.04E-2	2.038E-5

QIN-Breast-02 Summary

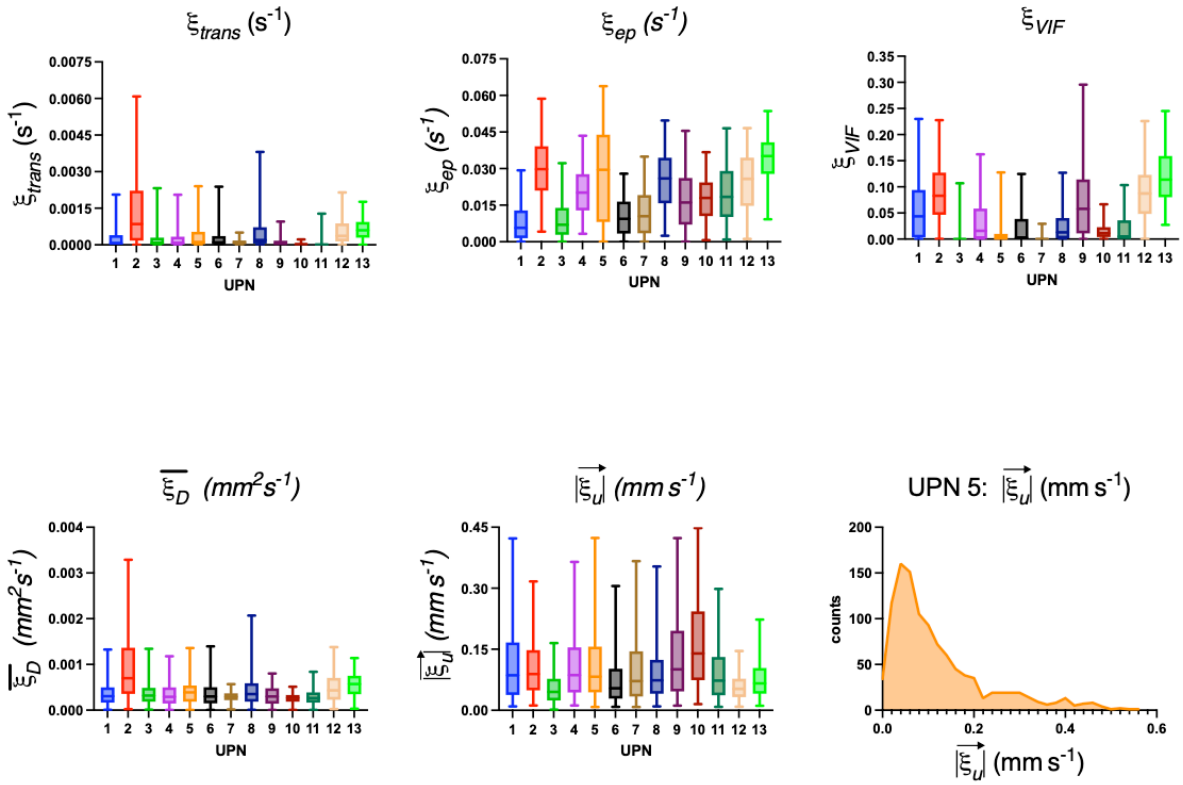

Supplemental figure 8: Summary of LCFR coefficients on the QIN Breast-02 DCE MRI dataset. The in-plane resolution of the voxels was 1.33 mm, and the slice-thickness was 5 mm. As the slice thickness was more than 2 times the in-plane resolution, the method was applied in 2 dimensions, neglecting the z-component of velocity- and diffusion- associated parameters. The results shown here, and in the tables below, are the results of analysis within a hand-drawn mask of enhancing tumor, and the logical intersection where the R^2 value of the method with respect to the weak-time derivative of the data is $R^2 > 0.5$.

Table S7: QIN Breast-02 Dataset Summary, Parameter Means

UPN	$\lvert\overrightarrow{\xi_u}\rvert$ (mm/s)	$\overline{\xi_D}$ (mm^2/s)	ξ_{VIF} (frac.)	ξ_{ep} (s^{-1})	ξ_{trans} (s^{-1})
1	1.19E-1	4.53 E-4	6.06E-2	7.99E-3	3.39E-4
2	1.09E-1	4.83 E-4	9.16 E-2	3.05E-2	1.50 E-3
3	5.67E-2	4.49 E-4	1.13 E-2	9.23E-3	3.08 E-4
4	1.12E-1	3.97E-4	3.48 E-2	2.08E-2	3.23 E-4
5	1.19E-1	4.12E-4	1.62 E-2	2.79E-2	4.27 E-4
6	8.02E-2	4.22E-4	2.36 E-2	1.06E-2	3.82 E-4
7	1.04E-1	4.45E-4	2.93E-3	1.20E-2	1.41 E-4
8	9.73E-2	3.48E-4	2.74E-2	2.55E-2	6.66 E-4
9	1.37E-1	4.90E-4	7.69E-2	1.74E-2	1.73 E-4
10	1.70E-1	4.81E-4	1.65E-2	1.76E-2	7.35 E-5
11	9.52E-2	4.57E-4	2.18E-2	2.00E-2	1.26E-4
12	5.89E-2	4.62E-4	9.04E-2	2.51E-2	5.83E-4
13	7.94E-2	4.64E-4	1.22E-1	3.39E-2	6.87E-4
Mean	1.02E-1	4.43E-4	4.59E-2	1.99 E-2	4.41E-4

Table S8: QIN Breast-02 Dataset Summary, Parameter 95% Confidence Interval

UPN	$\lvert\overrightarrow{\xi_u}\rvert$ (mm/s)	$\overline{\xi_D}$ (mm^2/s)	ξ_{VIF} (frac.)	ξ_{ep} (s^{-1})	ξ_{trans} (s^{-1})
1	2.68E-3	6.10E-6	1.69E-3	2.14E-4	1.32E-5
2	6.66E-4	1.93E-6	4.94E-4	1.13E-4	1.41E-5
3	1.32E-3	8.03E-6	8.68E-4	2.61E-4	1.70E-5
4	2.06E-3	6.02E-6	1.03E-3	2.39E-4	1.30E-5
5	3.23E-3	8.88E-6	1.07E-3	6.13E-4	2.00E-5
6	2.42E-3	7.24E-6	1.18E-3	2.74E-4	1.92E-5
7	1.69E-3	3.99E-6	1.37E-4	1.84E-4	2.53E-6
8	1.86E-3	4.88E-6	7.92E-4	2.86E-4	2.37E-5
9	1.35E-3	3.05E-6	9.44E-4	1.49E-4	3.63E-6
10	4.04E-3	5.65E-6	5.80E-4	3.29E-4	2.60E-6
11	1.47E-3	5.31E-6	5.90E-4	2.38E-4	5.96E-6
12	1.62E-3	9.93E-6	2.58E-3	5.61E-4	2.49E-5
13	1.73E-3	7.20E-6	1.73E-3	3.31E-4	1.48E-5
SD of Patient Mean	3.10E-2	3.97E-5	3.81E-2	8.41E-3	3.76E-4

References

1. J. M. Munson, R. V. Bellamkonda, M. A. Swartz, Interstitial Flow in a 3D Microenvironment Increases Glioma Invasion by a CXCR4-Dependent Mechanism. *Cancer Res.* **73**, 1536–1546 (2013).
2. U. Haessler, J. C. M. Teo, D. Foretay, P. Renaud, M. A. Swartz, Migration dynamics of breast cancer cells in a tunable 3D interstitial flow chamber. *Integr. Biol.* **4**, 401–409 (2012).
3. R. C. Cornelison, C. E. Brennan, K. M. Kingsmore, J. M. Munson, Convective forces increase CXCR4-dependent glioblastoma cell invasion in GL261 murine model. *Sci. Rep.* **8**, 17057 (2018).
4. J. D. Shields, M. E. Fleury, C. Yong, A. A. Tomei, G. J. Randolph, M. A. Swartz, Autologous Chemotaxis as a Mechanism of Tumor Cell Homing to Lymphatics via Interstitial Flow and Autocrine CCR7 Signaling. *Cancer Cell*. **11**, 526–538 (2007).
5. C. P. Ng, M. A. Swartz, Fibroblast alignment under interstitial fluid flow using a novel 3-D tissue culture model. *Am. J. Physiol. Circ. Physiol.* **284**, H1771–H1777 (2003).
6. A. C. Shieh, H. A. Rozansky, B. Hinz, M. A. Swartz, Tumor Cell Invasion Is Promoted by Interstitial Flow-Induced Matrix Priming by Stromal Fibroblasts. *Cancer Res.* **71**, 790–800 (2011).
7. L. M. Roberts, M. J. Perez, K. N. Balogh, G. Mingledorff, J. V. Cross, J. M. Munson, Myeloid Derived Suppressor Cells Migrate in Response to Flow and Lymphatic Endothelial Cell Interaction in the Breast Tumor Microenvironment. *Cancers (Basel).* **14**, 3008 (2022).
8. R. Li, J. C. Serrano, H. Xing, T. A. Lee, H. Azizgolshani, M. Zaman, R. D. Kamm, Interstitial flow promotes macrophage polarization toward an M2 phenotype. *Mol. Biol. Cell*. **29**, 1927–1940 (2018).
9. S. Kim, M. Chung, J. Ahn, S. Lee, N. L. Jeon, Interstitial flow regulates the angiogenic response and phenotype of endothelial cells in a 3D culture model. *Lab Chip*. **16**, 4189–4199 (2016).
10. K. C. Boardman, M. A. Swartz, Interstitial Flow as a Guide for Lymphangiogenesis. *Circ. Res.* **92**, 801–808 (2003).
11. O. M. Turk, R. C. Woodall, M. Gutova, C. E. Brown, R. C. Rockne, J. M. Munson, Delivery strategies for cell-based therapies in the brain: overcoming multiple barriers. *Drug Deliv. Transl. Res.* **11**, 2448–2467 (2021).
12. C. A. Stine, J. M. Munson, Convection-Enhanced Delivery: Connection to and Impact of Interstitial Fluid Flow. *Front. Oncol.* **9** (2019), doi:10.3389/fonc.2019.00966.
13. W. Schörner, M. Laniado, H. P. Niendorf, C. Schubert, R. Felix, Time-dependent changes in image contrast in brain tumors after gadolinium-DTPA. *AJNR. Am. J. Neuroradiol.* **7**, 1013–20 (1986).
14. R. Stupp, W. P. Mason, M. J. van den Bent, M. Weller, B. Fisher, M. J. B. Taphoorn, K. Belanger, A. A. Brandes, C. Marosi, U. Bogdahn, J. Curschmann, R. C. Janzer, S. K. Ludwin, T. Gorlia, A. Allgeier, D. Lacombe, J. G. Cairncross, E. Eisenhauer, R. O. Mirimanoff, Radiotherapy plus Concomitant and Adjuvant Temozolomide for Glioblastoma. *N. Engl. J. Med.* **352**, 987–996 (2005).
15. G. Shukla, G. S. Alexander, S. Bakas, R. Nikam, K. Talekar, J. D. Palmer, W. Shi, Advanced magnetic resonance imaging in glioblastoma: a review. *Chinese Clin. Oncol.* **6**, 40–40 (2017).
16. N. Hylton, Dynamic Contrast-Enhanced Magnetic Resonance Imaging As an Imaging

Biomarker. *J. Clin. Oncol.* **24**, 3293–3298 (2006).
17. P. S. Tofts, G. Brix, D. L. Buckley, J. L. Evelhoch, E. Henderson, M. V. Knopp, H. B. W. Lawsson, T.-Y. Lee, N. A. Mayr, G. J. M. Parker, R. E. Port, J. Taylor, R. M. Weisskoff, Estimating kinetic parameters from dynamic contrast-enhanced t1-weighted MRI of a diffusable tracer: Standardized quantities and symbols. *J. Magn. Reson. Imaging*. **10**, 223–232 (1999).
18. H. Chen, F. Li, X. Zhao, C. Yuan, B. Rutt, W. S. Kerwin, Extended graphical model for analysis of dynamic contrast-enhanced MRI. *Magn. Reson. Med.* **66**, 868–878 (2011).
19. D. Sainz-DeMena, W. Ye, M. Á. Pérez, J. M. García-Aznar, A finite element based optimization algorithm to include diffusion into the analysis of DCE-MRI. *Eng. Comput.* **38**, 3849–3865 (2022).
20. M. Pellerin, T. E. Yankeelov, M. Lepage, Incorporating Contrast Agent Diffusion Into the Analysis of DCE-MRI Data. *Magn. Reson. Med.* **58**, 1124–1134 (2007).
21. K. M. Kingsmore, A. Vaccari, D. Abler, S. X. Cui, F. H. Epstein, R. C. Rockne, S. T. Acton, J. M. Munson, MRI analysis to map interstitial flow in the brain tumor microenvironment. *APL Bioeng.* **2**, 031905 (2018).
22. Q. Zhang, P. Spincemaille, M. Drotman, C. Chen, S. Eskreis-Winkler, W. Huang, L. Zhou, J. Morgan, T. D. Nguyen, M. R. Prince, Y. Wang, Quantitative transport mapping (QTM) for differentiating benign and malignant breast lesion: Comparison with traditional kinetics modeling and semi-quantitative enhancement curve characteristics. *Magn. Reson. Imaging*. **86**, 86–93 (2022).
23. N. Sinno, E. Taylor, M. Milosevic, D. A. Jaffray, C. Coolens, Incorporating cross-voxel exchange into the analysis of dynamic contrast-enhanced imaging data: theory, simulations and experimental results. *Phys. Med. Biol.* **66**, 205018 (2021).
24. J. Zhao, Y. Cao, W. Liu, D. Han, Non-invasive assessment for intratumoural distribution of interstitial fluid flow. *Magn. Reson. Lett.* (2023), doi:10.1016/j.mrl.2023.03.001.
25. S. Walker-Samuel, T. A. Roberts, R. Ramasawmy, J. S. Burrell, S. P. Johnson, B. M. Siow, S. Richardson, M. R. Gonçalves, D. Pendse, S. P. Robinson, R. B. Pedley, M. F. Lythgoe, Investigating Low-Velocity Fluid Flow in Tumors with Convection-MRI. *Cancer Res.* **78**, 1859–1872 (2018).
26. A. Shukla-Dave, N. A. Obuchowski, T. L. Chenevert, S. Jambawalikar, L. H. Schwartz, D. Malyarenko, W. Huang, S. M. Noworolski, R. J. Young, M. S. Shiroishi, H. Kim, C. Coolens, H. Laue, C. Chung, M. Rosen, M. Boss, E. F. Jackson, Quantitative imaging biomarkers alliance (QIBA) recommendations for improved precision of DWI and DCE-MRI derived biomarkers in multicenter oncology trials. *J. Magn. Reson. Imaging*. **49**, e101–e121 (2019).
27. "QIBA Profile:3DCE-MRI Quantification (DCEMRI-Q)" (2020), (available at https://qibawiki.rsna.org/images/1/1f/QIBA_DCE-MRI_Profile-Stage_1-Public_Comment.pdf).
28. S. L. Brunton, J. L. Proctor, J. N. Kutz, Discovering governing equations from data by sparse identification of nonlinear dynamical systems. *Proc. Natl. Acad. Sci.* **113**, 3932–3937 (2016).
29. R. T. Woodall, P. Sahoo, Y. Cui, B. T. Chen, M. S. Shiroishi, C. Lavini, P. Frankel, M. Gutova, C. E. Brown, J. M. Munson, R. C. Rockne, Repeatability of tumor perfusion kinetics from dynamic contrast-enhanced MRI in glioblastoma. *Neuro-Oncology Adv.* **3** (2021), doi:10.1093/noajnl/vdab174.
30. D. A. Messenger, D. M. Bortz, Weak SINDy for partial differential equations. *J. Comput. Phys.* **443**, 110525 (2021).

31. T. BELYTSCHKO, The Finite Element Method: Linear Static and Dynamic Finite Element Analysis: Thomas J. R. Hughes. *Comput. Civ. Infrastruct. Eng.* **4**, 245–246 (2008).
32. K. Clark, B. Vendt, K. Smith, J. Freymann, J. Kirby, P. Koppel, S. Moore, S. Phillips, D. Maffitt, M. Pringle, L. Tarbox, F. Prior, The Cancer Imaging Archive (TCIA): Maintaining and Operating a Public Information Repository. *J. Digit. Imaging*. **26**, 1045–1057 (2013).
33. T. Yankeelov, G. Karczmar, R. Abramson, Data from QIN-BREAST-02[Dataset]. *Cancer Imaging Arch.* (2019), , doi:https://doi.org/10.7937/TCIA.2019.4cfm06rr.
34. T. S. Koh, S. Hartono, C. H. Thng, T. K. H. Lim, L. Martarello, Q. S. Ng, In Vivo Measurement of Gadolinium Diffusivity by Dynamic Contrast-Enhanced MRI : A Preclinical Study of Human Xenografts. *Magn. Reson. Med.* **69**, 269–276 (2013).
35. M. J. Gordon, K. C. Chu, A. Margaritis, A. J. Martin, C. R. Ethier, B. K. Rutt, Measurement of Gd-DTPA Diffusion Through PVA Hydrogel Using a Novel Magnetic Resonance Imaging Method. *Biotechnol. Bioeng.* **65**, 459–467 (1999).
36. T. Hompland, C. Ellingsen, K. M. Øvrebø, E. K. Rofstad, Interstitial Fluid Pressure and Associated Lymph Node Metastasis Revealed in Tumors by Dynamic Contrast-Enhanced MRI. *Cancer Res.* **72**, 4899–4908 (2012).
37. H. Dafni, T. Israely, Z. M. Bhujwalla, L. E. Benjamin, M. Neeman, Overexpression of Vascular Endothelial Growth Factor 165 Drives Peritumor Interstitial Convection and Induces Lymphatic Drain. *Cancer Res.* **62**, 6731–6739 (2002).
38. E. A. B. F. Lima, J. T. Oden, D. A. Hormuth, T. E. Yankeelov, R. C. Almeida, Selection, calibration, and validation of models of tumor growth. *Math. Model. Methods Appl. Sci.* **26**, 2341–2368 (2016).
39. E. A. B. F. Lima, J. T. Oden, B. Wohlmuth, A. Shahmoradi, D. A. Hormuth, T. E. Yankeelov, L. Scarabosio, T. Horger, Selection and validation of predictive models of radiation effects on tumor growth based on noninvasive imaging data. *Comput. Methods Appl. Mech. Eng.* **327**, 277–305 (2017).
40. A. B. Brummer, A. Xella, R. Woodall, V. Adhikarla, H. Cho, M. Gutova, C. E. Brown, R. C. Rockne, Data driven model discovery and interpretation for CAR T-cell killing using sparse identification and latent variables. *Front. Immunol.* **14** (2023), doi:10.3389/fimmu.2023.1115536.
41. J. I. Ausman, W. R. Shapiro, D. P. Rall, Studies on the Chemotherapy of Experimental Brain Tumors: Development of an Experimental Model. *Cancer Res.* **30**, 2394–2400 (1970).
42. C. Sandmann, E. Hodneland, J. Modersitzki, A practical guideline for T 1 reconstruction from various flip angles in MRI. *J. Algorithm. Comput. Technol.* **10**, 213–223 (2016).
43. K. Sung, B. L. Daniel, B. A. Hargreaves, Transmit B1+ field inhomogeneity and T 1 estimation errors in breast DCE-MRI at 3 tesla. *J. Magn. Reson. Imaging*. **38**, 454–459 (2013).
44. Y. Shen, F. L. Goerner, C. Snyder, J. N. Morelli, D. Hao, D. Hu, X. Li, V. M. Runge, T1 Relaxivities of Gadolinium-Based Magnetic Resonance Contrast Agents in Human Whole Blood at 1.5, 3, and 7 T. *Invest. Radiol.* **50**, 330–338 (2015).
45. S. L. Barnes, J. G. Whisenant, M. E. Loveless, T. E. Yankeelov, Practical Dynamic Contrast Enhanced MRI in Small Animal Models of Cancer: Data Acquisition, Data Analysis, and Interpretation. *Pharmaceutics*. **4**, 442–478 (2012).
46. A. L. Bendinger, C. Debus, C. Glowa, C. P. Karger, J. Peter, M. Storath, Bolus arrival time estimation in dynamic contrast-enhanced magnetic resonance imaging of small

animals based on spline models. *Phys. Med. Biol.* **64**, 045003 (2019).
47. A. Singh, R. K. S. S. Rathore, M. Haris, S. K. Verma, N. Husain, R. K. Gupta, Improved bolus arrival time and arterial input function estimation for tracer kinetic analysis in DCE-MRI. *J. Magn. Reson. Imaging*. **29**, 166–176 (2009).
48. T. S. Koh, S. Bisdas, D. M. Koh, C. H. Thng, Fundamentals of tracer kinetics for dynamic contrast-enhanced MRI. *J. Magn. Reson. Imaging*. **34**, 1262–1276 (2011).
49. T. E. Yankeelov, J. C. Gore, Dynamic Contrast Enhanced Magnetic Resonance Imaging in Oncology:Theory, Data Acquisition,Analysis, and Examples. *Curr. Med. Imaging Rev.* **3**, 91–107 (2007).
50. G. M. Conte, L. Altabella, A. Castellano, V. Cuccarini, A. Bizzi, M. Grimaldi, A. Costa, M. Caulo, A. Falini, N. Anzalone, Comparison of T1 mapping and fixed T1 method for dynamic contrast-enhanced MRI perfusion in brain gliomas. *Eur. Radiol.* **29**, 3467–3479 (2019).